FOXR2 Is an Epigenetically Regulated Pan-Cancer Oncogene That Activates ETS Transcriptional Circuits

Jessica W. Tsai[1,2,3], Paloma Cejas[4,5], Dayle K. Wang[1,3], Smruti Patel[6,7,8], David W. Wu[1], Phonepasong Arounleut[6], Xin Wei[6], Ningxuan Zhou[4,5], Sudeepa Syamala[4,5], Frank P.B. Dubois[1,9], Alexander Crane[1,9], Kristine Pelton[10], Jayne Vogelzang[10], Cecilia Sousa[10], Audrey Baguette[11,12], Xiaolong Chen[13], Alexandra L. Condurat[1,3], Sarah E. Dixon-Clarke[9,14], Kevin N. Zhou[1,3], Sophie D. Lu[1,3], Elizabeth M. Gonzalez[1,3], Madison S. Chacon[1,3], Jeromy J. Digiacomo[1,3], Rushil Kumbhani[1,3], Dana Novikov[1,3], J'Ya Hunter[1,3], Maria Tsoli[15], David S. Ziegler[15,16,17], Uta Dirksen[18,19], Natalie Jager[20,21,22], Gnana Prakash Balasubramanian[20,21], Christof M. Kramm[23], Michaela Nathrath[24,25], Stefan Bielack[26], Suzanne J. Baker[27], Jinghui Zhang[13], James M. McFarland[1], Gad Getz[1,28,29,30], François Aguet[1], Nada Jabado[31,32], Olaf Witt[20,22,33,34,35], Stefan M. Pfister[20,21,34,35], Keith L. Ligon[1,10,36], Volker Hovestadt[1,2,3], Claudia L. Kleinman[12,31], Henry Long[4,5], David T.W. Jones[20,21], Pratiti Bandopadhayay[1,2,3], and Timothy N. Phoenix[6]

ABSTRACT

Forkhead box R2 (*FOXR2*) is a forkhead transcription factor located on the X chromosome whose expression is normally restricted to the testis. In this study, we performed a pan-cancer analysis of *FOXR2* activation across more than 10,000 adult and pediatric cancer samples and found *FOXR2* to be aberrantly upregulated in 70% of all cancer types and 8% of all individual tumors. The majority of tumors (78%) aberrantly expressed FOXR2 through a previously undescribed epigenetic mechanism that involves hypomethylation of a novel promoter, which was functionally validated as necessary for FOXR2 expression and proliferation in *FOXR2*-expressing cancer cells. *FOXR2* promoted tumor growth across multiple cancer lineages and co-opted ETS family transcription circuits across cancers. Taken together, this study identifies FOXR2 as a potent and ubiquitous oncogene that is epigenetically activated across the majority of human cancers. The identification of hijacking of ETS transcription circuits by FOXR2 extends the mechanisms known to active ETS transcription factors and highlights how transcription factor families cooperate to enhance tumorigenesis.

Significance: This work identifies a novel promoter that drives aberrant FOXR2 expression and delineates FOXR2 as a pan-cancer oncogene that specifically activates ETS transcriptional circuits across human cancers.

See related commentary by Liu and Northcott, p. 2977

[1]Broad Institute of MIT and Harvard, Cambridge, Massachusetts. [2]Department of Pediatrics, Harvard Medical School, Boston, Massachusetts. [3]Department of Pediatric Oncology, Dana-Farber Boston Children's Cancer and Blood Disorders Center, Boston, Massachusetts. [4]Department of Medical Oncology, Dana-Farber Cancer Institute and Harvard Medical School, Boston, Massachusetts. [5]Center for Functional Cancer Epigenetics, Dana-Farber Cancer Institute, Boston, Massachusetts, Cancer Program, Broad Institute, Cambridge, Massachusetts. [6]Division of Pharmaceutical Sciences, James L. Winkle College of Pharmacy, University of Cincinnati, Cincinnati, Ohio. [7]Division of Pediatric Neurosurgery, Cincinnati Children's Hospital Medical Center, Cincinnati, Ohio. [8]Department of Neurosurgery, University of Cincinnati College of Medicine, Cincinnati, Ohio. [9]Department of Cancer Biology, Dana-Farber Cancer Institute, Boston, Massachusetts. [10]Department of Oncologic Pathology, Dana-Farber Cancer Institute, Harvard Medical School, Boston, Massachusetts. [11]Quantitative Life Sciences, McGill University, Montreal, Quebec H3A 2A7, Canada. [12]Lady Davis Research Institute, Jewish General Hospital, Montreal, Quebec H3T 1E2, Canada. [13]Department of Computational Biology, St. Jude Children's Research Hospital, Memphis, Tennessee. [14]Department of Biological Chemistry and Molecular Pharmacology, Boston, Massachusetts. [15]Children's Cancer Institute, Lowy Cancer Research Centre, University of New South Wales, Sydney, NSW, Australia. [16]School of Women's and Children's Health, University of New South Wales, Sydney, NSW, Australia. [17]Kids Cancer Centre, Sydney Children's Hospital, Randwick, NSW, Australia. [18]West German Cancer Center, Pediatrics III, University Hospital Essen, Essen, Germany. [19]German Cancer Consortium (DKTK), Essen/Düsseldorf, Germany. [20]Hopp Children's Cancer Center Heidelberg (KiTZ), Heidelberg University Hospital and German Cancer Research Center (DKFZ) Heidelberg, Germany. [21]Division of Pediatric Neuro-Oncology, German Cancer Research Center (DKFZ), Heidelberg, Germany. [22]German Cancer Consortium (DKTK), Heidelberg, Germany. [23]Division of Pediatric Hematology and Oncology, University Medical Center Göttingen, Göttingen, Germany. [24]Department of Pediatric Hematology and Oncology, Klinikum Kassel, Kassel, Germany. [25]Children's Cancer Research Centre and Department of Pediatrics, Klinikum rechts der Isar, Technische Universität München, Munich, Germany. [26]University Hospital Stuttgart, Stuttgart, Germany. [27]Department of Developmental Neurobiology, St. Jude Children's Research Hospital, Memphis, Tennessee. [28]Harvard Medical School, Boston, Massachusetts. [29]Department of Pathology, Massachusetts General Hospital, Boston, Massachusetts. [30]Center for Cancer Research, Massachusetts General Hospital, Boston, Massachusetts. [31]Department of Human Genetics, McGill University, Montreal, H3A 0C7, Canada. [32]Department of Pediatrics, McGill University, and The Research Institute of the McGill University Health Centre, Montreal, H4A 3J1, Canada. [33]Clinical Cooperation Unit Pediatric Oncology, German Cancer Research Center (DKFZ), Heidelberg, Germany. [34]Department of Pediatric Oncology, Hematology, Immunology, and Pulmonology, Heidelberg University Hospital, Heidelberg, Germany. [35]National Center for Tumor Disease (NCT) Network, Germany. [36]Department of Pathology, Brigham and Women's Hospital, Boston, Massachusetts.

D.T.W. Jones, P. Bandopadhayay, and T.N. Phoenix equally and jointly supervised this article.

Corresponding Authors: Timothy N. Phoenix, James L. Winkle College of Pharmacy, University of Cincinnati, 231 Albert Sabin Way, Medical Sciences Building Room 3005M, Cincinnati, OH 45267. Phone: 513-558-7749; E-mail: phoenity@ucmail.uc.edu; Pratiti Bandopadhayay, Dana-Farber Cancer Institute, 450 Brookline Avenue, Mayer Building Room 658, Boston, MA 02215. Phone: 617-632-3000; E-mail: Pratiti_Bandopadhayay@dfci.harvard.edu; and David T.W. Jones, Hopp Children's Cancer Center Heidelberg (KiTZ), German Cancer Research Center (DKFZ), Im Neuenheimer Feld 280, Heidelberg 69120, Germany. Phone: 49-6221-424675; E-mail: David.Jones@kitz-heidelberg.de

Cancer Res 2022;82:2980–3001

doi: 10.1158/0008-5472.CAN-22-0671

Introduction

Elucidating how aberrant transcription factors (TF) hijack normal developmental and cellular pathways to induce oncogenesis is a critical question in oncology. Forkhead box (FOX) proteins are a superfamily of transcriptional regulators that are highly evolutionarily conserved and share a forkhead DNA-binding domain (1). These TFs play broad roles in cellular homeostasis, and their expression is exquisitely controlled in adult tissues. Within this large family of TFs, *Forkhead Box R2* (*FOXR2*), located on the X chromosome, has been implicated as an oncogene in a subset of cancers (2–6). However, there has yet to be a systematic characterization of the oncogenic role of *FOXR2* across all cancers, and the mechanisms through which it induces tumor formation have not been fully elucidated. Although *FOXR2* has been shown to be activated through structural variants in CNS (6) and peripheral neuroblastomas (5), the expression profile of *FOXR2* across all cancers and the different genetic and epigenetic mechanisms of activating *FOXR2* expression have not yet been explored. Moreover, the patterns and regulation of *FOXR2* expression in normal tissues are unknown.

The mechanisms through which *FOXR2* enhances tumor formation have also not been systematically evaluated. Prior work has largely focused on the role of *FOXR2* in stabilizing MYC isoforms (5, 7), but it remains unknown whether *MYC* represents the sole interactor in facilitating *FOXR2* function. FOXR2 expression has been associated with activation of several pathways within specific lineages (3, 4); however, the direct targets of FOXR2 as a forkhead box family TF have not been comprehensively mapped across cancers. TFs typically exert their effects by cooperating within transcriptional complexes. Indeed, some TFs, including other forkhead box family members (8–12), have been shown to mediate their effects through direct dimerization with other TFs or by colocalization at distinct DNA motifs. It is unknown whether similar mechanisms contribute to *FOXR2*-mediated oncogenesis.

To address these questions, we performed an analysis of *FOXR2* expression across a cohort of human cancers encompassing newly generated and previously published adult (13, 14) and pediatric (15–18) data sets. We found evidence of *FOXR2* expression in 8% of tumors, representing more than 70% of all cancer types and identified distinct mechanisms of *FOXR2* activation, including a novel nonstructural variant mechanism accounting for the majority of *FOXR2*-expressing cancers. Notably, we uncovered an association between *FOXR2* and activation of E26 transformation-specific (ETS) transcription factor circuits and found that ETS TFs are required for *FOXR2*-mediated transformation. These findings highlight a previously underrecognized role of *FOXR2* as a potent oncogene across human cancers and demonstrate how TFs from different families cooperate to induce oncogenesis.

Materials and Methods

Data sets

All studies were performed in accordance with the Declaration of Helsinki.

1. Pan-cancer evaluation of FOXR2 expression across patient samples included multiple sources. These include the following.

A. INFORM consortium: RNA sequencing (RNA-seq) data from a cohort of high-risk pediatric malignancies were assessed for aberrant *FOXR2* expression and for evidence of fusion transcripts involving *FOXR2*. These samples were collected through the INFORM personalized medicine study (https://www.kitz-heidelberg.de/en/inform) as previously described (16, 18). Written informed consent was obtained from patients and/or guardians for use of tissue for research through protocols approved by the Institutional Review Board (IRB) at each participating center. The study is registered with the German Clinical Trial Register, number DRKS00007623.

B. Dana-Farber Cancer Institute: Whole-genome and RNA-seq data from a recently generated cohort of pediatric high-grade gliomas (HGG) and diffuse midline gliomas (15) were analyzed to evaluate for FOXR2 expression and associated genetic features such as single-nucleotide and structural variants. These samples were collected with written informed consent from patients and/or guardians through protocols approved by the IRB at Dana-Farber Cancer Institute.

C. St Jude: To examine the transcriptome profiles of FOXR2 in HGG, we accessed RNA-seq data available in St. Jude Cloud (17). In total, RNA-seq data of (189) samples of HGG were identified using the St. Jude Cloud data portal (https://platform.stjude.cloud/data/diseases) on August 5, 2021. The data were preprocessed and aligned using an internal pipeline within the cloud using genome build hg19. FPKM were then manually calculated using DESeq2(V1.30.1). Written informed consent was obtained from patients and/or legal guardians for use of tissue for research through protocols approved by the IRB at St. Jude Children's Research Hospital.

D. The Cancer Genome Atlas (TCGA): We downloaded RNA-SeqV2 data for FOXR2 using cBioPortal (19). RSEM data were downloaded in October 2021. Additionally, raw transcriptome HTSeq counts for TCGA-SKCM and TCGA-LUSC (lung squamous cancer) were downloaded in October 2021 using the TCGAbiolinks (RRID:SCR_017683; refs. 20–22) and GDC (RRID:SCR_014514; ref. 23) api method.

2. Normal tissues

A. GTEx: The data (testis BAM files) used for the analyses described in this manuscript were obtained from the GTEx Portal (RRID:SCR_013042; ref. 24) in March 2021 and the V7 release (dbGaP accession number phs000424.v7) on AnVIL (https://anvil.terra.bio/).

B. ENCODE: We downloaded the following bed files from the Encode Project (RRID:SCR_015482; http://www.encodeproject.org; ref. 25) in October 2021 with the following identifiers: ENCFF883MWF (ENCAN060PZM, ENCSR926NMC), ENCFF717CEO_(ENCAN842IOM, ENCXR143MZL), ENCFF988KVL (ENCAN09INZE, ENCSR224STY), ENCFF557NJX (ENCAN444UAU, ENCSR936FAH), ENCFF475YJU (ENCAN394PDR, ENCSR000ATH), ENCFF755ZOL (ENCAN800QUV, ENCSR847AIA), ENCFF190JDV (ENCAN172OEV, ENCSR000AOQ), ENCFF888OII (ENCAN604KGT, ENCSR081OTO), ENCFF863USS (ENCAN357XIX, ENCSR550WUX), and ENCFF082ZYU (ENCAN689IGS, ENCSR000APH).

3. Cancer cell lines

A. Cancer Cell Line Encyclopedia (CCLE; RRID:SCR_013836): RNA-seq BAM files were downloaded from NCBI SRA PRJNA523380 in February 2021. The following accession numbers were

obtained: LN428_CENTRAL_NERVOUS_SYSTEM (SRX5414856, SRR8615544), KMH2_HAEMATOPOIETIC_AND_LYMPHOID_TISSUE (SRX5415142, SRR8615908), KYSE150_OESOPHAGUS (SRX5415016, SRR8616034), NCIH2227_LUNG (SRX5414938, SRR8616112), HCC4006_LUNG (SRX5414298, SRR8615455), CHP126_AUTONOMIC_GANGLIA (SRX5414227, SRR8615526), HT1080 (SRX5415007, SRR8616043), A375_SKIN (SRX5415030, SRR8616020), U266B1_HAEMATOPOIETIC_AND_LYMPHOID_TISSUE (SRX5415154, SRR8615896), SKNFI_AUTONOMIC_GANGLIA (SRX5415110, SRR8615940), MKN1_STOMACH (SRX5414235, SRR8615518), GRANTA519_HAEMATOPOIETIC_AND_LYMPHOID_TISSUE (SRX5414373, SRR8615380), KPNSI9S_AUTONOMIC_GANGLIA (SRX5414979, SRR8616071), MDAMB435S_SKIN (SRX5414817, SRR8615583), HS294T_SKIN (SRX5414339, SRR8615414), KMS27_HAEMATOPOIETIC_AND_LYMPHOID_TISSUE (SRX5414405, SRR8615348), 8MGBA_CENTRAL_NERVOUS_SYSTEM (SRX5414753, SRR8615647), A101D_SKIN (SRX5414754, SRR8615646), HT144_SKIN (SRX5415003, SRR8616047), WM88_SKIN (SRX5417212, SRR8618303), A2058_SKIN (SRX5414763, SRR8615637), H4_CENTRAL_NERVOUS_SYSTEM (SRX5414365, SRR8615388), SKNAS_AUTONOMIC_GANGLIA (SRX5414251, SRR8615502), SKNSH_AUTONOMIC_GANGLIA (SRX5414247, SRR8615506), HS944T_SKIN (SRX5415161, SRR8615889), HCC1438_LUNG (SRX5414585, SRR8615815), NCIH838_LUNG (SRX5415074, SRR8615976), HCC202_BREAST (SRX5414875, SRR8616175), NCIH1155_LUNG (SRX5414800, SRR8615600), MOLP2_HAEMATOPOIETIC_AND_LYMPHOID_TISSUE (SRX5414984, SRR8616066), SIMA_AUTONOMIC_GANGLIA (SRX5414725, SRR8615675), SHP77_LUNG (SRX5414726, SRR8615674), DAOY_CENTRAL_NERVOUS_SYSTEM (SRX5415088, SRR8615962), TT_THYROID (SRX5414674, SRR8615726), LN18_CENTRAL_NERVOUS_SYSTEM (SRX5414562, SRR8615838), LCLC103H_LUNG (SRX5414935, SRR8616115), SNU8_OVARY (SRX5414275, SRR8615478), NCIH358_LUNG (SRX5414595, SRR8615805), NCIH2882_LUNG (SRX5414211, SRR8615542), NIHOVCAR3_OVARY (SRX5414308, SRR8615445), GCT_SOFT_TISSUE (SRX5414367, SRR8615386), M059K_CENTRAL_NERVOUS_SYSTEM (SRX5414639, SRR8615761), RPMI7951_SKIN (SRX5414316, SRR8615437), IGR1_SKIN (SRX541455, SRR8615845), KMS21BM_HAEMATOPOIETIC_AND_LYMPHOID_TISSUE (0.01pt?>SRX5414403, SRR8615350), A4FUK_HAEMATOPOIETIC_AND_LYMPHOID_TISSUE (SRX5415034, SRR8616016), JHH4_LIVER (SRX5415131, SRR8615919), NCIH446_LUNG (SRX5414589, SRR8615811), KNS60_CENTRAL_NERVOUS_SYSTEM (SRX5414698, SRR8615702), ONCODG1_OVARY (SRX5414523, SRR8615230), NCIH1836_LUNG (SRX5414791, SRR8615609), MDAMB361_BREAST (SRX5414819, SRR8615581), KLE_ENDOMETRIUM (SRX5415143, SRR8615907).

B. DepMap: Data for genome-wide CRISPR-Cas9 knockout screens for FOXR2, genome-wide RNAi screens for FOXR2, and FOXR2 expression were downloaded from the Cancer Dependency Map Portal (depmap.org/portal; ref. 26) in October 2021. FOXR2 $\log_2(\text{TPM} + 1)$ expression was utilized from the DepMap 21Q3 Public release (27).

Analyses of RNA-seq and whole-genome sequencing

RNA-seq analysis

Human tumors: For INFORM data sets, pediatric glioma (TPM) and osteosarcoma (FPKM) expression matrices were analyzed in gene set enrichment analysis (GSEA; RRID:SCR_003199) using the Broad Institute desktop GSEA Java application. Analysis parameters included 1,000 permutations and phenotype labels based on FOXR2 expression or lack of FOXR2 expression. False discovery rate (FDR) cutoff of q value < 0.05 was utilized for significantly enriched gene sets in pediatric gliomas [diffuse midline gliomas (DMG) and hemispheric gliomas], whereas FDR cutoff of q value < 0.25 was utilized for osteosarcomas. Within each cancer type, the random module in Python was utilized to generate random integers. These randomly selected tumors were permuted as FOXR2 expressing to confirm that enrichment of significant gene sets was specific to FOXR2 expression.

For TCGA data sets, SKCM and LUSC tumors were analyzed using raw TCGA counts and comparing FOXR2-expressing tumors to non-FOXR2-expressing tumors. Raw FOXR2 count greater than or equal to 10 was used as the cutoff for determining FOXR2 expression. Differential gene expression testing was performed by DESeq2 (v1.32.0; RRID:SCR_015687) in R (version 4.1.0) and RStudio (version 1.4.1717). Normalized counts were subsequently used to perform GSEA using the Fast GSEA (fgsea, RRID:SCR_020938) package in R (version 4.1.0) and RStudio (version 1.4.1717). Analysis parameters included 10,000 permutations and phenotype labels based on FOXR2 expression or lack of FOXR2 expression. FDR cutoff of q value < 0.05 was utilized for significantly enriched gene sets in TCGA tumors.

Mouse IUE tumors: Freshly isolated tumors were snap-frozen, and total RNA was isolated using the NucleoSpin RNA kit (Macherey-Nagel, 740955). RNA quality control was performed on a Bioanalyzer (Bio-Rad) to ensure the quality of each sample submitted. For isolation of polyA RNA, a NEBNext Poly(A) mRNA Magnetic Isolation Module (New England BioLabs, E7490) was used for polyA RNA purification with a total of 1 μg good quality total RNA as input. The SMARTer Apollo NGS Library Prep System (Takara Bio, 640078) was used for automated polyA RNA isolation. For RNA-seq library preparation, the library for RNA-seq was prepared by using the NEBNext Ultra II Directional RNA Library Prep Kit for Illumina (New England BioLabs, E7760). After indexing via PCR enrichment (8 cycles), the amplified libraries together with the negative control were cleaned up for quality control analysis. To study differential gene expression, individually indexed and compatible libraries were proportionally pooled (∼25 million reads per sample in general) for clustering in the cBot system (Illumina, SY-301-2002). Libraries at the final concentration of 15 pmol/L were clustered onto a single-read flow cell using the TruSeq SR Cluster Kit v3 (Illumina, GD-401-3001), and sequenced to 51 bp using the TruSeq SBS Kit v3 (Illumina, FC-401-3001) on the Illumina HiSeq system. Sequence reads were aligned to the reference genome using the TopHat aligner (RRID:SCR_013035), and reads aligning to each known transcript were counted using Bioconductor packages for next-generation sequencing data analysis.

Differential gene expression testing was performed by DESeq2 (v1.22.1; RRID:SCR_015687). Normalized counts were subsequently used to perform GSEA using the Fast GSEA (fgsea) package in R (version 4.1.0) and RStudio (Version 1.4.1717). Analysis parameters included 10,000 permutations and phenotype labels based on FOXR2 expression or lack of FOXR2 expression. FDR cutoff of q value < 0.05 was utilized for significantly enriched gene sets in cell lines.

Cell lines

RNA-seq was performed by the Molecular Biology Core Facilities at Dana-Farber Cancer Institute. Libraries were prepared using

KAPA mRNA HyperPrep (Roche, KK8581) strand specific sample preparation kits from 200 ng of purified total RNA according to the manufacturer's protocol on a Beckman Coulter Biomek i7. The finished dsDNA libraries were quantified by Qubit Fluorometer (Thermo Fisher) and 4200 TapeStation system (Agilent, G2991BA). Uniquely dual indexed libraries were pooled in an equimolar ratio and shallowly sequenced on an Illumina MiSeq to further evaluate library quality and pool balance. The final pool was sequenced on an Illumina NovaSeq 6000 targeting 40 million 150-bp read pairs per library at the Dana-Farber Cancer Institute Molecular Biology Core Facilities.

Sequenced reads were aligned to the UCSC hg19 reference genome assembly and gene counts were quantified using STAR (v2.7.3a, RRID:SCR_004463). Differential gene expression testing was performed by DESeq2 (v1.22.1, RRID:SCR_015687). RNA-seq analysis was performed using the VIPER snakemake pipeline (28). Normalized counts were subsequently used to perform GSEA using the Fast GSEA (fgsea) package in R (version 4.1.0) and RStudio (Version 1.4.1717). Analysis parameters included 10,000 permutations and phenotype labels based on FOXR2 expression or lack of FOXR2 expression. FDR cutoff of q value < 0.05 was utilized for significantly enriched gene sets in cell lines.

Whole-genome sequencing analysis of pHGGs

Somatic nucleotide variants and structural variants were annotated from our recently completed analyses of 179 pediatric whole-genome sequences (15).

Identification of novel promoters using RNA-seq

RNA-seq BAM files were visualized using Integrative Genomics Viewer (IGV, RRID:SCR_011793). Novel promoters were identified by visualization of sequencing from tumors and cancer cell lines in comparison with RefSeq hg19 and testicular RNA-seq data from GTEx (24).

Identification of FOXR2 structural variants

RNA-seq BAM files were visualized using Integrative Genomics Viewer (IGV, RRID:SCR_011793). FOXR2 fusion breakpoints were identified by showing soft-clipped bases (Preferences, Alignments) and visualizing read pairs using split screen function.

Correlation of CpG methylation with FOXR2 expression in CCLE lines

1. Reduced representation bisulfite sequencing analysis

Reduced representation bisulfite sequencing (RRBS) data for 916 cell lines in the CCLE, RRID:SCR_013836; refs. 14, 29) was obtained from the Sequence Read Archive (SRA, accession ID PRJNA523380) and reprocessed. Briefly, each cell line's RRBS bam file was converted into its respective fastq file with Samtools v1.12 (RRID:SCR_002105; ref. 30) and realigned to the hg38 reference genome with bismark v0.23.0 (RRID:SCR_005604; ref. 31) using manually specified parameters -D 20 -R 3 -N 1. All other parameters were left at their default setting. To quantify the methylation of each individual CpG locus, bismark aligned bam files were analyzed with the processBismarkAln function from the R package MethylKit (RRID:SCR_005177; ref. 32) with parameters mincov = 5 and minqual = 20.

2. FOXR2 gene expression data

FOXR2 gene expression [$\log_2$(TPM + 1)] were taken from the 21Q3 DepMap (RRID:SCR_017655) public gene expression data, obtained from the DepMap Portal (https://depmap.org/portal/download/; ref. 27).

3. Correlation analysis of FOXR2 expression and DNA methylation

To determine the significance between DNA methylation within the FOXR2 topologically associated domain (TAD) and FOXR2 gene expression, we considered all CpG loci on the X chromosome that had a defined methylation measurement in at least 50 cell lines. Each surviving methylation measurement (cell line, CpG loci) was then normalized by calculating its z-score relative to the distribution of methylation values for all cell lines in that CpG loci. Next, the Pearson correlation coefficient was calculated between FOXR2 expression and each surviving CpG locus.

4. Generation of the heatmap

Z-scored methylation values for all CpG loci in the FOXR2 TAD were visualized in the heatmap. To reduce the sparsity of the RRBS data, the data were smoothed for each CpG loci by setting the methylation of a CpG locus in a given cell line to the average of the CpG locus and the five CpG loci before and after.

5. Quantification of the methylation differences in the FOXR2 TAD between FOXR2 high and low cell lines

To generate a FOXR2 TAD-level methylation score for each CCLE cell line, the Z-scored methylation values of all nonempty CpG loci in a given cell line were averaged together. CCLE cell lines were then binned into two categories, those that express low levels of FOXR2 and those that express high levels of FOXR2. An expression level of 0.20 ($\log_2$(TPM + 1)) was used as the cutoff to call high FOXR2-expressing cell lines. All other cell lines were called low FOXR2-expressing.

Chromatin immunoprecipitation sequencing

1. Sample preparation and sequencing

For histone marks profiling, cells were crosslinked with 1 mL of 1% formaldehyde for 10 minutes. For CTCF and HA profiling cells were crosslinked in two steps with 2 mmol/L of disuccinimidyl glutarate (DSG, Pierce) for 45 minutes at room temperature followed by 1 mL of 1% formaldehyde for 10 minutes. Crosslinked cells were then quenched with 0.125 M glycine for 5 minutes at room temperature and washed with PBS. After fixation, pellets were resuspended in 500 μL of 1% SDS (50 mmol/L Tris-HCl pH 8, 10 mmol/L EDTA) and sonicated for 5 minutes (histone marks) or 10 minutes (HA and CTCF) using a Covaris E220 instrument (setting: 140 peak incident power, 5% duty factor and 200 cycles per burst) in 1 mL AFA fiber millitubes. Chromatin was immunoprecipitated with 10 μg of each antibody (H3K4me3 Abcam ab8580, RRID:AB_306649; H3K27ac Diagenode C15410194, RRID:AB_2637079; CTCF Millipore 07-729, RRID:AB_441965; HA Abcam ab9110, RRID:AB_307019). Five μg of chromatin was used for histone mark chromatin immunoprecipitations (ChIP), and 40 μg of chromatin was used for HA and CTCF ChIPs. ChIP sequencing (ChIP-seq) libraries were made using the NEBNext Ultra II DNA Library Prep Kit (New England BioLabs, E7103). 75 bp paired-end reads were sequenced on a NextSeq instrument (Illumina).

2. ChiP-seq analysis and peak calling

A modified version of the ChiLin pipeline was used for quality control and preprocessing of the data (33). We used Burrows-Wheeler Aligner (BWA Version: 0.7.17-r1188, RRID:SCR_010910) as a read

mapping tool to align to hg19 using default parameters. Unique reads for a position for peak calling were used to reduce false-positive peaks, and statistically significant peaks were finally selected by calculating a FDR of reported peaks. ChIP-seq peaks were called using MACS2 (v2.1.2) with a cutoff of FDR<0.01 for H3K27ac and H3K4me3, FDR<0.1 for HA. DESeq2 (RRID: SCR_015687) was used to identify differential peaks in ChIP-seq, where gained or lost peaks were defined with the threshold of log2 fold change of 1 or 2 and an adjusted $P < 0.05$. Principal component analysis was performed using princomp in R.

Cis-regulatory element annotation system (CEAS) analysis was used to annotate resulting peaks with genome features. Cistrome Toolkit (dbtoolkit.cistrome.org; RRID:SCR_000242; refs. 34–36) was used to probe which factors might regulate the user-defined genes. Genomic Regions Enrichment of Annotations Tool (GREAT; RRID: SCR_005807) was used to annotate peaks with their biological functions. Conservation plots were obtained with the Conservation Plot (version 1.0.0) tool available in Cistrome. CTCF quality control metrics are available in Supplementary Table S1.

3. Visualization of ChIP-seq data

Read depth normalized profiles corresponding to read coverage per 1 million reads were used for heatmaps and for visualization using the Integrative Genomics Viewer (IGV, RRID:SCR_011793). Heat maps were prepared using deepTools (version 2.5.4; RRID:SCR_016366; ref. 37) and aggregation plots for ChIP-seq signals were generated using Sitepro in CEAS.

Plasmid generation

Luciferase reporter

A lentiviral firefly luciferase reporter system was constructed from pGL4.25 (Promega) and the pLKO.1 backbone using Gibson Assembly. The DNA sequence of the Exon −3 promoter was cloned into the lentiviral firefly reporter vector using KpnI and NheI restriction sites. Ligation was performed using the Quick Ligase Kit (New England Biolabs, M2200). Calf intestinal alkaline phosphatase (New England Biolabs, M0290) was used for dephosphorylation of the vector to prevent recircularization during ligation. Constitutively active pLX13-*Renilla* (Addgene, 118016, RRID:Addgene_118016) was used as an intrinsic control.

Overexpression vectors

FOXR2 wild-type (WT), HA-FOXR2 WT, ΔMYC, and ΔForkhead constructs were synthesized as Gateway compatible entry clones (pENTR11) by GenScript. Entry clone sequences were confirmed using attL1, CTACAAACTCTTCCTGTTAGTTAG; attL2, ATGGCTCATAACACCCCTTG. The sequences in the Gateway entry vectors were then cloned into pLX312 destination vectors using the Gateway LR Clonase II reaction (Life Technologies, 11791-020) per the manufacturer's instructions. pLX312-HcRed and pLX312-lacZ plasmids were cloned from pLX307-HcRed (RRID: Addgene_117732) and pLX307-lacZ (RRID:Addgene_117730). Destination vector sequences were confirmed using EF-1 alpha, TCAAGCCTCAGACAGTGGTTC; WPRE, CATAGCGTAAAAGGAGCAACA.

All-in-one CRISPR-Cas9 KO (pXPR_023) and all-in-one CRISPR interference (dCas9-KRAB; pXPR_066) vectors were utilized for CRISPR-Cas9 experiments. Circular pXPR vectors were obtained from the Broad Institute Genetic Perturbation Platform (GPP). Circular pXPR vectors were cut using BsmBI (New England Biolabs, R0739S) and NEB Buffer 3.1 (New England Biolabs, B7203S). This reaction was incubated at 55°C for four hours. Loading dye was added to the digested product, then loaded onto a 1% agarose gel. The open vector was subsequently excised and extracted using the QIAquick Gel Extraction Kit (Qiagen, 28706×4).

Oligonucleotides were designed using CRISPick tool. Forward oligos were designed to have additional 5′ overhang 5′ CACCG, whereas reverse oligos were designed to have 5′ overhang AAAC and 3′ overhang C to allow ligation with the digested pXPR vector. Oligonucleotide sequences used in this study: sgRNA_1^{Cas9}, GTGCCCCCTTGGCAGCCAGG; sgRNA_2^{Cas9}, AGCCCCCACAAAAAGACGAA; sgRNA_3^{Cas9}, CGAAGGGTCTAACTGCTCAG; sgRNA_4^{Cas9}, TGTGAGCTCAAAGTCACTGG; sgRNA_1^{KRAB}, TCGCATGTGTCGCCATAATA; sgRNA_2^{KRAB}, AGAAGAGAAATACCCTATTA; sgRNA_3^{KRAB}, AGGGTATTTCTCTTCTCTAG; sgRNA_4^{KRAB}, CTGGTCAATTCTGCGACATC; lacZ, AACGGCGGATTGACCGTAAT. LentiCRISPRv2GFP (RRID:Addgene_82416) was used as a CRISPR/Cas9 control.

Oligos were annealed using a PCR cycling machine with incubation at 95°C for 5 minutes, 70°C for 5 minutes, and then temperature decreasing by 5°C every 5 minutes until room temperature (25°C). Next, annealed oligos were ligated to the open vectors using 10X Ligase Buffer (New England Biolabs, B0202S) and T4 Ligase (New England Biolabs, M0202L). Ligation proceeded at 16°C for 4 hours. Following ligation, the ligation reaction was added to 25 μL of Invitrogen One Shot Stbl3 chemically competent E. coli (Invitrogen, C737303). The reaction was placed on ice for 30 minutes. Heat shock was performed at 42°C for 45 seconds, followed by incubation on ice for 2 minutes. SOC media (Invitrogen, 15544034) were subsequently added to recovered cells for recovery and then placed at 37°C for 1 hour on a shaker. Transformants were plated on Luria-Bertani agar plates containing 100 μg/mL of carbenicillin for selection. Cells were grown at 37°C while shaking for no more than 14 hours.

Minipreps were performed using the QIAprep Spin Miniprep Kit (Qiagen, 27104). Sequences were verified by Etonbio using the U6 primer (GACTATCATATGCTTACCGT). Once sequences were verified, Maxipreps were inoculated and performed using the ZymoPURE II Plasmid Maxiprep Kit (Zymo Research, D4202).

Cell line models

Primary neural stem cell cultures were established from the medial ganglionic eminence of embryonic day 14 murine embryos. Mouse neural stem cells (mNSC) were propagated in cultures as neurospheres in media containing a 1:1 ratio of DMEM/F-12 (Invitrogen, 11330-032) and Neurobasal-A (Invitrogen, 10888-022) with 10% each of HEPES Buffer Solution 1 M (Thermo Fisher, 15630080), sodium pyruvate solution 100 nmol/L (Life Technologies, 11360070), MEM nonessential amino acids solution 10 mmol/L (Thermo Fisher, 11140050), Glutamax-I Supplement (Thermo Fisher, 35050061), and penicillin/streptomycin solution (Life Technologies, 15140122). Media was supplemented with B27 minus Vitamin A (Invitrogen, 12587-010), epidermal growth factor (EGF, StemCell Tech Inc., 78006), fibroblast growth factor (FGF, StemCell Tech Inc., 78003), and heparin solution 0.2% (StemCell Tech Inc., 07980). Neurospheres were dissociated using Accutase (StemCell Tech Inc., 07922) and passaged every four days.

Human H9-derived neural stem cells (hNSC) are derived from the NIH approved H9 (WA09) human embryonic stem cells (Gibco, N7800-100). hNSCs were propagated in cultures on plates pretreated for at least one hour with Geltrex LDEV-Free Reduced Growth Factor Basement Membrane Matrix (Gibco, A1413201). hNSCs were grown

in media containing a 1:1 ratio of DMEM/F-12 (Invitrogen, 11330-032) and Neurobasal-A (Invitrogen, 10888-022) with 10% each of HEPES Buffer Solution 1 M (Thermo Fisher, 15630080), sodium pyruvate solution 100 nmol/L (Life Technologies, 11360070), MEM nonessential amino acids solution 10 mmol/L (Thermo Fisher, 11140050), Glutamax-I Supplement (Thermo Fisher, 35050061), and penicillin/streptomycin solution (Life Technologies, 15140122). Media was supplemented with B27 minus vitamin A (Invitrogen, 12587-010), EGF, StemCell Tech Inc., 78006), FGF, StemCell Tech Inc., 78003), and heparin solution 0.2% (StemCell Tech Inc., 07980). Accutase (StemCell Tech Inc., 07922) was used to detach cells from Geltrex plates.

Cell lines included in this study included DIPG-IV (RRID:CVCL_IT39), DIPG-XIII (RRID:CVCL_IT41), BT245 (RRID:CVCL_IP13), NCI-H838 (RRID:CVCL_1594), A375 (RRID:CVCL_0132), mNSCs, hNSCs, and AALE cells. AALE cells were provided by the Meyerson Lab. AALE cells were grown in SABM Small Airway Epithelial Cell Growth Basal Medium (Lonza, CC-3119) supplemented with SAGM Small Airway Epithelial Cell Growth Medium SingleQuots (Lonza, CC-4124). BT245 was grown in tumor stem media containing a 1:1 ratio of DMEM/F-12 (Invitrogen, 11330-032) and Neurobasal-A (Invitrogen, 10888-022) with 10% each of HEPES Buffer Solution 1 M (Thermo Fisher, 15630080), sodium pyruvate solution 100 nmol/L (Life Technologies, 11360070), MEM nonessential amino acids solution 10 mmol/L (Thermo Fisher, 11140050), Glutamax-I Supplement (Thermo Fisher, 35050061), and penicillin/streptomycin solution (Life Technologies, 15140122). Media was supplemented with B27 minus Vitamin A (Invitrogen, 12587-010), EGF, StemCell Tech Inc., 78006), FGF, StemCell Tech Inc., 78003), and heparin solution 0.2% (StemCell Tech Inc., 07980). DIPG-IV and DIPG-XIII were grown in tumor stem media containing a 1:1 ratio of DMEM/F-12 (Invitrogen, 11330-032) and Neurobasal-A (Invitrogen, 10888-022) with 10% each of HEPES Buffer Solution 1 M (Thermo Fisher, 15630080), sodium pyruvate solution 100 nmol/L (Life Technologies, 11360070), MEM nonessential amino acids solution 10 mmol/L (Thermo Fisher, 11140050), Glutamax-I Supplement (Thermo Fisher, 35050061), and penicillin/streptomycin solution (Life Technologies, 15140122). Media was supplemented with B27 minus vitamin A (Invitrogen, 12587-010), EGF, StemCell Tech Inc., 78006), FGF, StemCell Tech Inc., 78003), PDGF-AA (Shenandoah Biotech, 100-16), PDGF-BB (Shenandoah Biotech, 100-18), and heparin solution 0.2% (StemCell Tech Inc., 07980). Neurospheres were dissociated using Accutase (StemCell Tech Inc., 07922) and passaged every 4 days. NCI-H838 (NSCLC) were grown adherently in RPMI with 10% serum. Cells were dissociated with Trypsin-EDTA 0.25% (Gibco, 25200056). A375 (SKCM) was grown in DMEM with 10% serum.

Cell lines were routinely fingerprinted for validation of identity using SNP-based and STR fingerprinting assays. These fingerprinting assays were compared with a database of prior fingerprinting assay and reference STRs. Cells were tested every three months for *Mycoplasma* infection using the MycoAlert Mycoplasma Detection Kit (Lonza, LT07-318), according to manufacturer's instructions.

Lentiviral production and transductions

Virus production

HEK293T (RRID:CVCL_0063) cells were transfected with 10 μg of lentiviral expression vectors with packaging plasmids encoding PSPAX2 and VSVG using Lipofectamine 3000 (Thermo Fisher, L3000075). Supernatant containing lentivirus was collecting 24 hours following transfection and concentrated using Lenti-X Concentrator (Takara, 631231) according to the manufacturer's instructions.

Transductions

mNSCs, DMG cell lines, A375, and NCI-H838 were infected using a spinfection protocol (2,000 RPM for 120 minutes at 30°C without polybrene) in 12-well plates (Corning, 3513). For GFP-positive pLX_312 vectors, infected cells were subsequently flow sorted for GFP-positive cells within 48 hours after the infection. For CRISPR KO and CRISPR interference experiments, cells were selected using puromycin selection in pXPR_023 and pXPR_066 vector-expressing cells (0.5 μg/mL for H9 hNSCs, 0.75 μg/mL for DIPG-IV, 1 μg/mL for A375, and 1 μg/mL for NCI-H838) 24 hours after the infection. No infection controls were used for every infection, and cells were removed from puromycin selection after 48 hours.

DIPG-IV, NCI-H838, and A375 were infected with all-in-one plasmids (pXPR_023) expressing Cas9 and four independent guides against FOXR2 Exon 1 and a control guide against eGFP. DIPG-IV, NCI-H838, and A375 were infected with all-in-one plasmids (pXPR_066) expressing dCas9-KRAB and four independent guides against FOXR2 Exon 1 and a control guide against lacZ. One day after infection, cells were selected in puromycin (DIPG-IV 0.75 μg/mL puromycin, NCI-H838, and A375 1 μg/mL puromycin) for 48 hours.

Luciferase reporter assay

Reporter experiments were conducted in both NCI-H838 and A375 cell lines constitutively expressing pLX13-*Renilla* luciferase. Cells were infected first with pLX13-*Renilla* luciferase and underwent hygromycin selection for 7 days (NCI-H838 250 μg/mL hygromycin, A375 350 μg/mL hygromycin). Once *Renilla*-expressing cell lines were established, cells were then infected with the cloned firefly Exon −3 reporter (or control). One day after infection, cells were selected in puromycin (NCI-H838 and A375 1 μg/mL puromycin) for 48 hours. Following selection, cells were plated at 750 cells per well in white-bottom 96-well plates (Corning, 3917). The Dual-Glo Luciferase Assay (Promega) was used following the manufacturer's protocols, and plates were read on day 7 following puromycin selection. The firefly luciferase reading was normalized to the constitutive *Renilla* luciferase signal.

In vitro proliferation assays

In vitro proliferation assays were performed using the IncuCyte live cell imaging system (Sartorius). For neurospheres including mNSCs and all DMG cell lines, cells were plated for IncuCyte immediately after selection into ULA 96-well plates (Corning, 7007). Neurospheres were plated at 1,000 cells per well, and the plate was spun at 200 × *g* for 15 minutes at room temperature to facilitate spheroid formation. ULA 96-well plates were then analyzed in the IncuCyte using the spheroid assay. Adherent cells (A375, NCI-H838) were plated into 24-well adherent plates (Corning, 3524) and analyzed in the IncuCyte using the adherent assay. H9 hNSCs were plated into 48-well adherent plates (Corning, 3548) that were pretreated with Geltrex LDEV-Free Reduced Growth Factor Basement Membrane Matrix (Gibco, A1413201) and analyzed over time using the adherent assay in the IncuCyte live-cell imaging system.

In utero brainstem electroporation

All animal experiments were performed according to protocols approved by the Institutional Animal Care and Use Committee at the University of Cincinnati.

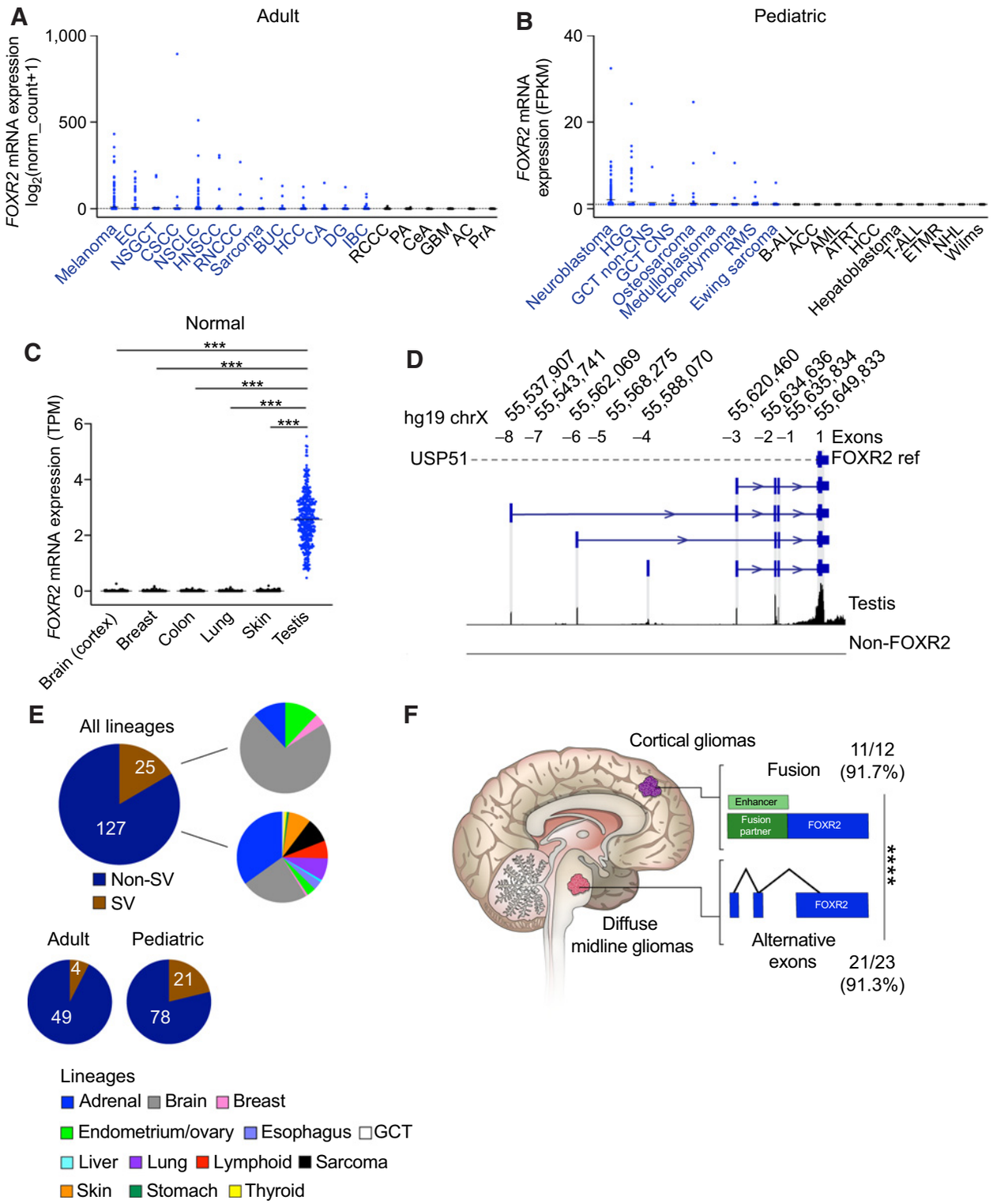

Figure 1.

FOXR2 is aberrantly expressed across adult and pediatric cancers through multiple mechanisms. **A,** *FOXR2* mRNA expression $\log_2$(normalized count + 1) generated by RSEM of all TCGA samples across cancer subtypes ($n = 8{,}391$). Mean expression for each cancer subtype is indicated by a black horizontal line. Cancer subtypes labeled blue indicate mean FOXR2 expression > 0.1. Cancer subtypes: melanoma ($n = 443$); EC, endometrial cancer ($n = 230$); NSGCT, nonseminomatous germ cell tumor ($n = 86$); CSCC, cervical squamous cell carcinoma ($n = 248$); (*Continued on the following page.*)

Time-pregnant CD-1 IGS (Charles River, #022) were used for all experiments. *In utero* electroporation (IUE) was performed as previously described (38, 39). Approximately, 1 μL of concentrated DNA plasmid mixtures (concentrated to 1 μg/μL for each plasmid) containing 0.05% Fast Green was injected into either the lateral ventricles (for cortical targeted) or fourth ventricle (for brainstem targeted) of e13.5–14.5 embryos using a pulled glass capillary pipette. Injected embryos were electroporated by applying 5 square pulses (45V, 50-ms pulses with 950 ms intervals) with 3-mm tweezer electrodes directed toward the dorsal cortex (lateral ventricle injections) or lower rhombic lip (fourth ventricle injections; BTX/Harvard Bioscience). Embryos were returned to the abdominal cavity, incision was sutured, and the female was monitored until fully recovered. Subsequently, successfully electroporated offspring, identified by bioluminescent imaging (Xenogen), were monitored regularly, and mice presenting symptoms related to tumor burden were euthanized according to protocols approved by the Institutional Animal Care and Use Committee at the University of Cincinnati.

DNA plasmids used include PBCAG-PdgfraD842V-Ires-eGFP, PBCAG-DNp53-Ires-Luciferase, PBCAG-H3f3aK27M-Ires-eGFP, PBCAG-PdgfraWT-Ires-eGFP, PBCAG-FOXR2-Ires-eGFP, PBCAG-V5-FOXR2 WT-Ires-eGFP, PBCAG-V5ΔMYC-FOXR2-Ires-eGFP, PBCAG-V5ΔForkhead-FOXR2-Ires-eGFP; pCAG-PBase.

Quantitative reverse transcription PCR

RNA was isolated using the Qiagen RNeasy kit (Qiagen, 74106) with on-column DNase digestion (Qiagen, 79256). The Superscript II Reverse Transcriptase Kit (Invitrogen, 18064014) was used to make cDNA from RNA. Gene expression was subsequently quantified using the Power SYBR Green Master Mix (Applied Biosystems, 4367659). FOXR2 expression values were normalized to vinculin, and the fold change was calculated using the delta-delta Ct method (ddCt). The following primers were used and ordered from Integrated DNA Technologies (IDT): *h-FOXR2*-1-Forward, TGGCAAATCAACAACCAAGA; *h-FOXR2*-1-Reverse, GTCTGGCACCTTCTCAAAGC; *h-FOXR2*-2-Forward, AGCCCAGTGGAAAAGAGGAT; *h-FOXR2*-2-Reverse, TTCATTTCAGGGGACTGGAG; Vinculin-Forward, CGATACCACAACTCCCATCAA, Vinculin-Reverse, AGCTGCCCTCTCATCAAATAC.

Immunoblotting

Cells were lysed in RIPA buffer containing protease and phosphatase inhibitors on ice for 1 hour. Lysates were subsequently centrifuged at 17,000 × *g* for 15 minutes at 4°C, and the supernatant was obtained. The supernatant was quantified with Pierce 660 nm Protein Assay (Thermo Fisher, 22660). After quantification, the supernatant was mixed with 4× SDS loading buffer, and subsequently heated at 95°C for 5 minutes then subjected to SDS-PAGE on NuPAGE 4%–12% Bis-Tris gradient gels (Invitrogen, NP0321). Blots were also loaded with Precision Plus Protein Western C standards (Bio-Rad, 1610376) Blots were dry transferred using the iBlot2 Dry Blotting System (Thermo Fisher, IB21001), then placed in block (5% milk in TBST) at room temperature for 1 hour while shaking. Blots were probed with primary antibody overnight, then washed three times with TBST. Antibodies against the following proteins were used in this study: FOXR2 (Proteintech, 14111-1-AP, RRID:AB_2878015), vinculin-HRP (Santa Cruz, SC 73614, RRID:AB_1131294), HA-Tag Rabbit mAb (Cell Signaling, 3724, RRID:AB_1549585), anti-c-Myc (Abcam, ab32072, RRID:AB_731658), ETS1 rabbit mAb (Cell Signaling, 14069, RRID:AB_2798383), and ETV3 rabbit polyclonal (Bethyl, A303-736A, RRID:AB_11205284). Blots were then probed with secondary antibody (anti-rabbit IgG, HRP-linked antibody, Cell Signaling, 7074, RRID:AB_2099233) for one hour at room temperature before application of SuperSignal West Pico PLUS chemiluminescent substrate (Thermo Fisher, 34578) and subsequent imaging on a FujiFilm LAS-4000.

Quantification of Western immunoblots

Raw Western blot images were imported into Photoshop (Adobe 22.4.2 Release, RRID:SCR_014199). Image color was inverted, and then the luminosity (gray value mean) of each band was recorded. Luminosity for each band was normalized to its corresponding vinculin band. The mean and SEM of three replicates were used for each experiment.

IHC and immunofluorescence

IUE brain tumors were collected for paraffin and frozen sections. For histopathology, brain samples were fixed overnight in 10% formalin (FisherScientific, SF100-4) and then transferred into 70% ethanol before being processed for paraffin embedding. Five-micrometer-thick sections were prepared on a microtome and processed for hematoxylin-eosin staining. Stained slides were scanned at 20× on a Aperio digital slide scanner.

Samples collected for frozen sections were perfused with cold PBS followed by 4% paraformaldehyde (PFA; Electron Microscopy Sciences, 15710) and post-fixed overnight in 4% PFA. The next day,

(*Continued.*) NSCLC ($n = 994$); HNSCC, head and neck squamous cell carcinoma ($n = 515$); RNCCC, renal nonclear cell carcinoma ($n = 348$); sarcoma ($n = 253$); BUC, bladder urothelial carcinoma ($n = 407$); HCC, hepatocellular carcinoma ($n = 363$); CA, colorectal adenocarcinoma ($n = 365$); DG, diffuse glioma ($n = 513$); IBC, invasive breast carcinoma ($n = 1{,}082$); RCCC, renal clear cell carcinoma ($n = 510$); PA, pancreatic adenocarcinoma ($n = 177$); CeA, cervical adenocarcinoma ($n = 46$); GBM, glioblastoma ($n = 160$); AC, adrenocortical carcinoma ($n = 78$); PrA, prostate adenocarcinoma ($n = 460$). Black dotted line, $\log_2$(normalized count + 1) > 1. **B,** *FOXR2* mRNA expression FPKM scores across pediatric cancer subtypes within the INFORM data set ($n = 1{,}279$). Mean expression for each cancer subtype is indicated by black horizontal line. Cancer subtypes labeled blue indicate mean *FOXR2* expression > 1.0. Cancer subtypes: neuroblastoma ($n = 162$); HGG, high-grade glioma ($n = 209$); GCT non-CNS, germ cell tumor, noncentral nervous system ($n = 21$), GCT CNS, germ cell tumor, central nervous system ($n = 9$), osteosarcoma ($n = 137$), medulloblastoma ($n = 66$); ependymoma ($n = 92$); RMS, rhabdomyosarcoma ($n = 181$); Ewing sarcoma ($n = 147$); B-ALL, B-lymphoblastic leukemia ($n = 64$); ACC, adrenocortical carcinoma ($n = 8$); AML, acute myeloid leukemia ($n = 34$); ATRT, atypical teratoid rhabdoid tumor ($n = 21$); HCC, hepatocellular carcinoma ($n = 13$); hepatoblastoma ($n = 14$); T-ALL, T-lymphoblastic leukemia ($n = 16$); ETMR, embryonal tumor with multilayered rosettes ($n = 13$); NHL, non-Hodgkin lymphoma ($n = 28$); Wilms tumor ($n = 44$). Black dotted line, FPKM > 0. **C,** Normal postnatal expression of *FOXR2* from the GTEx data set. Mean and individual TPM values are displayed. ***, $P < 0.0001$ (Tukey multiple comparisons test). Lineages include the following: brain (cortex; $n = 255$), breast ($n = 459$), colon ($n = 779$), lung ($n = 578$), skin ($n = 1{,}304$), testis ($n = 361$). **D,** *FOXR2* isoforms identified in normal testis, which harbor additional exons to the single exon annotated in RefSeq (Exon +1). The position of each additional exon is shown, with the corresponding annotation used throughout this manuscript to refer to each of them: Exon −1, Exon −2, Exon −3, Exon −4, Exon −5, Exon −6, and Exon −7. Aligned reads from a non–*FOXR2*-expressing glioma are shown as a negative control. **E,** The proportion of *FOXR2*-expressing tumors identified to harbor SVs across 152 tumors encompassing all adult and pediatric lineages. Also shown are the different lineages represented in SV and non-SV *FOXR2*-expressing tumors. **F,** Fraction and percentage of tumors within each brain location are shown that harbor SVs or aberrant promoters to activate *FOXR2*. SVs are enriched in cortical tumors whereas midline gliomas tend to activate FOXR2 through the use of aberrant promoters. ****, $P < 0.0001$ as determined by Fisher exact test for mutual exclusivity.

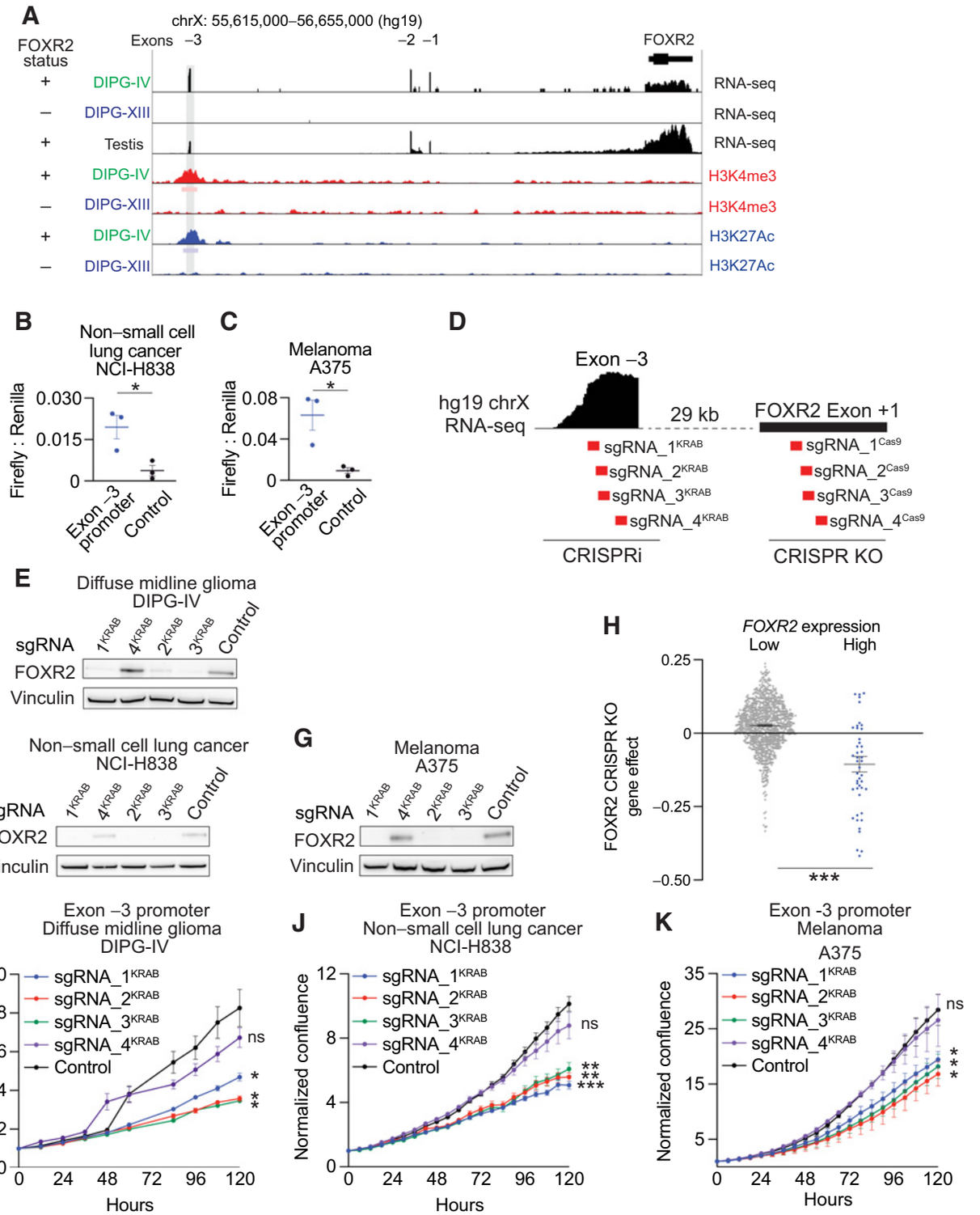

Figure 2.

FOXR2 is necessary in *FOXR2*-expressing cancers. **A,** Top three tracks: Expression and structure of *FOXR2* isoforms in *FOXR2*-expressing DIPG-IV diffuse midline glioma (DMG) cells (green), non–*FOXR2*-expressing DIPG-XIII DMG cells (blue), and normal testis (black), as determined by RNA-seq. Bottom four tracks: H3K4me3 promoter and H3K27ac enhancer binding in the same *FOXR2*-expressing DIPG-IV DMG and non–*FOXR2*-expressing DIPG-XIII DMG cells. Bars below the H3K4me3 and H3K27ac ChIP-seq tracks indicate the position of statistically enriched peaks (FDR < 0.01). The position of Exon-3 is depicted with a gray bar across the different tracks. (*Continued on the following page.*)

samples were washed multiple times in PBS and then transferred into a 30% sucrose/PBS solution for 24–48 hours at 4°C. Cryoprotected samples were embedded and frozen in tissue freezing media (Ted Pella, 27300), and then cut as 50-μm-thick free-floating sections on a cryostat (Lecia). Sections are stored at 4°C in a PBS + 0.005% sodium azide solution prior to staining. For immunofluorescent staining, sections are incubated in blocking solution: PBS + 0.5% Triton X-100 (Sigma, X) + 10% normal donkey serum (EMD Millipore, S30-100ML) at room temperature for 1 hour prior to addition of primary antibodies, which are then incubated overnight at 4°C on a rocking platform. The next day, sections are washed in PBS (5 × 5 minutes) and then transferred into blocking solution with the appropriate secondary antibodies and incubated at 4°C overnight. Sections are washed again in PBS (5 × 5 minutes) and next incubated with DAPI (Thermo Fisher, 62248) or Hoechst (Thermo Fisher, H3570) diluted 1:1,000 in PBS for 10 minutes. After final PBS washes, sections are mounted onto slides (FisherScientific Superfrost, 12-550-15) and coverslipped (Prolong Gold Antifade; Thermo Fisher, P36930). Primary antibodies used for staining included: eGFP (Aves, #GFP1020; 1:2,000 dilution, RRID: AB_10000240), Olig2 (Millipore, #Ab9610; 1:500 dilution, RRID: AB_570666), Gfap (Cell Signaling, #12389; 1:500 dilution, RRID: AB_2631098), Ki67 (Cell Signaling, #9129; 1:1,000 dilution, RRID: AB_2687446), and FOXR2 (ProteinTech, #14111-1-AP; 1:250 dilution, RRID:AB_2878015). Secondary antibodies conjugated to Alexa-fluorophores were purchased from Jackson ImmunoResearch or Thermo Fisher. Images were acquired on a confocal microscope (Nikon A1), and image analysis and editing were performed in ImageJ (NIH).

Cycloheximide assays

Cells were treated with 50 μg/mL cycloheximide (Sigma-Aldrich, C4859), and cell pellets were collected at the following time points: 0 minutes, 30 minutes, 1 hour, 2 hours, 3 hours, 4 hours, and 5 hours. Upon collection, cells were immediately lysed in RIPA buffer containing protease and phosphatase inhibitors on ice for 1 hour. Lysates were subsequently centrifuged at 17,000 × *g* for 15 minutes at 4°C, and the supernatant was obtained. Once all lysates were obtained and quantified, lysates were subjected to SDS-PAGE on NuPAGE 4%–12% Bis-Tris gradient gels (Invitrogen, NP0321) as described above.

Fluorescence-activated cell sorting

Cells were passaged as per routine cell culture methods and then resuspended in Flow Cytometry Staining Buffer (eBioscience, 00-4222-26). Gating was based on GFP expression, and non-GFP-expressing cells were used as negative controls for appropriate gating. Cells were subsequently flow sorted on a BD FACSAria II directly into 6-well plates containing media.

Statistical methods used throughout paper

Statistical analyses were performed in GraphPad Prism (9.1.2, RRID:SCR_002798). Statistical significance was determined by Fisher exact test, two-tailed unpaired *t* tests, log-rank Mantel–Cox test, or one-way ANOVA as described in the figure legends. All cell growth experiments were based on at least three independent experiments. *P* values < 0.05 were considered significant.

Data availability

RNA-seq from mouse models and cell lines in addition to ChIP-seq from cell lines have been deposited to GEO under accession number GSE206484. Whole-genome and RNA-seq of pediatric HGG samples (15) have been deposited to dbGaP with restricted access under accession number phs002380.v1.p1.

Results

FOXR2 is aberrantly expressed across adult and pediatric cancers

We analyzed *FOXR2* expression in more than 10,000 tumors across multiple cancer lineages including TCGA (n = 8,391; ref. 13) and pediatric (15–18) data sets (n = 1,884) to fully characterize the landscape of *FOXR2* expression across human cancers. We found *FOXR2* to be expressed in 71% (35/49) of all cancer lineages, collectively representing 8% of all tumors (844/10,275; **Fig. 1A** and **B**). *FOXR2* expression was most frequently observed in adult cancers that included melanoma (SKCM), endometrial cancer (EC), and non–small cell lung cancers (NSCLC), whereas in pediatric cancers, *FOXR2* was highly expressed in neuroblastoma (5), pediatric brain tumors including DMGs, and sarcomas. In contrast to its widespread activation across cancers, *FOXR2* expression is absent in nearly all normal postnatal human tissues. Analysis of *FOXR2* expression across normal autopsy samples (24) revealed lineage-restricted expression in the testis, with several splice variants observed (**Fig. 1C** and **D**). These data indicate that cancers aberrantly activate the expression of *FOXR2*.

FOXR2 is expressed through multiple mechanisms

Within cohorts of *FOXR2*-expressing tumors in pediatric (99/1884; INFORM, Dana-Farber Cancer Institute, and St. Jude's) and adult data sets (53/1739, CCLE cancer cell lines), the majority of *FOXR2*-

(*Continued.*) **B,** Firefly to *Renilla* luciferase relative light unit (RLU) ratio in *FOXR2*-expressing NCI-H838 NSCLC cells transduced with reporter constructs that harbor the Exon −3 promoter sequence relative to vector control. *, $P < 0.05$, as determined by a two-tailed unpaired *t* test comparing Exon −3 promoter sequence to control at 7 days following selection across three independent replicate experiments. **C,** Firefly to *Renilla* luciferase RLU ratio in *FOXR2*-expressing A375 melanoma (SKCM) cells transduced with reporter constructs that harbor the Exon −3 promoter sequence relative to vector control. *, $P < 0.05$, as determined by two-tailed unpaired *t* test comparing Exon −3 promoter sequence to control at 7 days following selection across three independent replicate experiments. **D,** Schematic showing the location of CRISPR interference guides (red, labeled sgRNA_1^{KRAB}, sgRNA_2^{KRAB}, sgRNA_3^{KRAB}, and sgRNA_4^{KRAB}) in relation to the *FOXR2* Exon −3 promoter peak. Four CRISPR-Cas9 KO guides targeting the FOXR2 Exon +1 are also shown. **E–G,** Representative Western immunoblots showing FOXR2 protein levels following transduction with CRISPRi lentivirus with guides targeting different regions of the *FOXR2* Exon −3 promoter peak, or nontargeting vector control using lysates derived from the following *FOXR2*-expressing cancer cell lines DIPG-IV DMGE (**E**), NCI-H838 NSCLC (**F**), and A375 melanoma (SKCM; **G**). **H,** Gene effect (*y*-axis) following *FOXR2* ablation in genome-scaled CRISPR-Cas9 loss-of-function screens across 948 cancer cell lines with low vs. high levels of *FOXR2* expression (*x*-axis). Values depict mean ± SEM. ***, $P < 0.0001$, as determined by two-tailed unpaired *t* test. **I,** CRISPR interference of *FOXR2* using sgRNA_1-4^{KRAB} in *FOXR2*-expressing DIPG-IV DMG cell line attenuates proliferation. Values indicate mean ± SEM across three replicate experiments. *, $P < 0.05$, as determined by two-tailed unpaired *t* tests comparing each guide relative to nontargeting control at 120 hours. **J,** Normalized confluence (relative to day 0) of *FOXR2*-expressing NCI-H838 NSCLC cells following transduction with CRISPRi vectors and guides targeting the Exon −3 *FOXR2* promoter. Values indicate mean ± SEM across three replicate experiments. **, $P < 0.01$; ***, $P < 0.001$ as determined by two-tailed unpaired *t* tests at 120 hours. **K,** Normalized confluence (relative to day 0) of *FOXR2*-expressing A375 melanoma (SKCM) cells following transduction with CRISPRi vectors and guides targeting the Exon −3 *FOXR2* promoter. Values indicate mean ± SEM across three replicate experiments. *, $P < 0.05$ as determined by two-tailed unpaired *t* tests at 120 hours. ns, not significant.

expressing pediatric (78.8%) and adult (92.5%) tumors did not harbor detectable activating somatic genetic events. Notably, the *FOXR2* mRNA structure in these tumors was different from the single exon depicted in the RefSeq *FOXR2* annotation and included additional exons upstream to the annotated promoter, similar to FOXR2 isoforms detected in RNA-seq of the normal testis (Supplementary Fig. S1A). The profiles of each of these isoforms varied across cancer lineages, with the presence of two to four additional upstream exons observed across tumor types. Almost all transcripts harbored two common upstream exons on Xp11.21, which we designated Exon −1, and chrX: 55,634,636-55,634,694, Exon −2.

Previous studies have reported structural variants (SV) involving *FOXR2* in CNS (6) and peripheral (5) neuroblastomas. However, within our cohorts of pediatric and adult *FOXR2*-expressing tumors, only 21.2% (21/99) and 7.5% (4/53) of tumors, respectively, harbored SVs involving FOXR2 (**Fig. 1E**). In each case, the SVs resulted in the juxtaposition of genes that are normally expressed within each respective lineage (Supplementary Fig. S1B) to upstream exons of *FOXR2* that are not included in the canonical RefSeq model (**Fig. 1D**). This observation suggests that SVs result in enhancer hijacking to promote expression of full-length *FOXR2*. Indeed, analysis of H3K27ac and H3K4me3 marks across normal samples in Encode (25, 40, 41) revealed the SV breakpoints to be associated with enhancers or promoters in all cases (Supplementary Table S2).

Within gliomas, our analysis revealed subsets of both cortical and midline HGG to harbor aberrant expression of *FOXR2* induced by either SVs or the Exon −3 promoter. Intriguingly, these mechanisms appear to exhibit regional specificity within the brain. Although cortical gliomas were more likely to harbor SVs, DMGs were enriched with tumors that expressed *FOXR2* through transcriptional activation from Exon −3 ($P < 0.0001$, Fisher exact test, **Fig. 1F**).

The Exon −3 promoter is sufficient to induce transcription and necessary for *FOXR2*-expressing cancer cells

The *FOXR2* transcription start site varied across lineages in non-SV FOXR2-expressing tumors. The most consistent finding across tumors was the presence of an aberrant start site at position chrX: 55,620,460–55,620,615 (hg19; Exon −3, Supplementary Fig. S1A), which was present in almost 78% of all *FOXR2*-expressing tumors (118/152). Based on the similarity of RNA structures to those found in normal testis, we reasoned that Exon −3 may represent the canonical promoter for *FOXR2*. We evaluated the H3K4me3 promoter landscape of FOXR2-expressing DMG cells using ChIP-seq. Indeed, we observed enrichment of an H3K4me3 promoter peak that colocalized with Exon −3 (**Fig. 2A**). This promoter peak was also associated with enrichment of H3K27ac enhancer binding, suggesting a transcriptionally active region (**Fig. 2A**). To further evaluate Exon −3 as an active promoter, we interrogated 13,976 ChIP-seq data sets (34–36, 42) and identified 22 TFs that bind to this region. These include transcription complex members POLR2A, KDM1A, BRD4, H2AZ, and BRD2, further supporting Exon −3 to represent an active promoter region (Supplementary Fig. S2A).

To functionally validate the promoter activity of Exon −3, we generated a luciferase reporter system whereby Firefly luciferase expression is driven by the Exon −3 promoter with an internal *Renilla* luciferase control. The Exon −3 promoter showed significant Firefly to *Renilla* luciferase activity in both NSCLC and SKCM cancer cell lines compared with the reporter construct without the promoter insert ($P < 0.05$, *t* test; **Fig. 2B** and **C**). These data demonstrate the Exon −3 promoter is indeed sufficient to drive transcription.

We leveraged CRISPR interference (CRISPRi; ref. 43) assays to functionally validate Exon −3 as the canonical *FOXR2* promoter that is necessary for FOXR2 expression (**Fig. 2D**). *FOXR2*-expressing DMG, NSCLC, and SKCM cell lines with start sites at Exon −3 were transduced with lentiviral dCas9-KRAB and guide RNAs (sgRNA) targeting four regions of Exon −3 or LacZ controls. Across all lines, transduction of the three sgRNAs targeting the most upstream sequence of Exon −3 was sufficient to suppress FOXR2 protein expression compared with controls ($P < 0.05$ all comparisons, **Fig. 2E–G**; Supplementary Fig. S2B–S2D; Supplementary Table S3). These sgRNAs also suppressed *FOXR2* RNA expression, assessed by both qRT-PCR (Supplementary Fig. S2E–S2G) and RNA-seq (Supplementary Fig. S2H–S2J). However, a fourth guide (sgRNA_4^{KRAB}), targeting the most downstream sequence of the four guides had no effect on FOXR2 expression ($P > 0.05$ all comparisons, **Fig. 2E–G**; Supplementary Fig. S2B–S2G; Supplementary Table S3). These findings confirm that the Exon −3 promoter is necessary for FOXR2 expression across lineages and represents an alternative transcription start site.

We next sought to determine whether the novel FOXR2 promoter is also necessary for the proliferation of *FOXR2*-expressing cancer cells. FOXR2 (Exon +1) has been reported to be necessary for the proliferation of *FOXR2*-expressing malignant peripheral nerve sheath tumors (2), breast cancer mouse xenografts (7), U251 adult glioma cells, and neuroblastoma cells (5). Indeed, interrogation of genome-scale CRISPR-Cas9 and RNAi screens performed across 948 and 525 cancer cell lines, respectively (26, 27, 44), revealed FOXR2 to be the top dependency in *FOXR2*-expressing cell lines ($P < 0.0001$ for CRISPR-Cas9 and RNAi, *t* test; **Fig. 2H**, Supplementary Fig. S3A, Supplementary Tables S3 and S4). Suppression of the Exon −3 promoter using CRISPRi in multiple lineages (DMG, NSCLC, and SKCM) was associated with the reduced proliferation of *FOXR2*-expressing models (**Fig. 2I–K**). Suppression of Exon +1 using CRISPR KO in multiple lineages was also associated with reduced proliferation (**Fig. 2D**; Supplementary Fig. S3B–S3D).

Activation of the aberrant FOXR2 promoter is associated with hypomethylation

We next sought to further delineate the mechanisms that lead to activation of the FOXR2 Exon-3 promoter. *FOXR2* is located on the X chromosome and its normal expression is restricted to the testis, analogous to numerous cancer/testis antigens (CTA) that are frequently expressed in several types of cancer (45–47). CTAs have been previously reported to be aberrantly activated through DNA hypomethylation (48). We reasoned that similar mechanisms may also drive aberrant *FOXR2* expression. To address this, we interrogated RRBS across 916 cancer cell lines from the CCLE collection, including 84 *FOXR2*-expressing and 832 nonexpressing lines (14, 29, 49). Indeed, we found that *FOXR2* expression was specifically anticorrelated with methylation levels of CpG sites within a region encompassing FOXR2 (FDR < 0.05 for Pearson correlations for each CpG site within this region; **Fig. 3A** and Supplementary Table S5). We also quantified levels of CpG methylation within the FOXR2 TAD of each cell line by averaging the methylation values of all CpG loci in a given cell line and found that *FOXR2*-expressing cell lines had significantly lower methylation scores compared with non–*FOXR2*-expressing cell lines ($P = 1.965e{-}15$, Welch *t* test; **Fig. 3B**). Further analyses leveraging Welch and hypergeometric tests confirmed that the methylation of CpG sites within the region surrounding *FOXR2* were most significantly

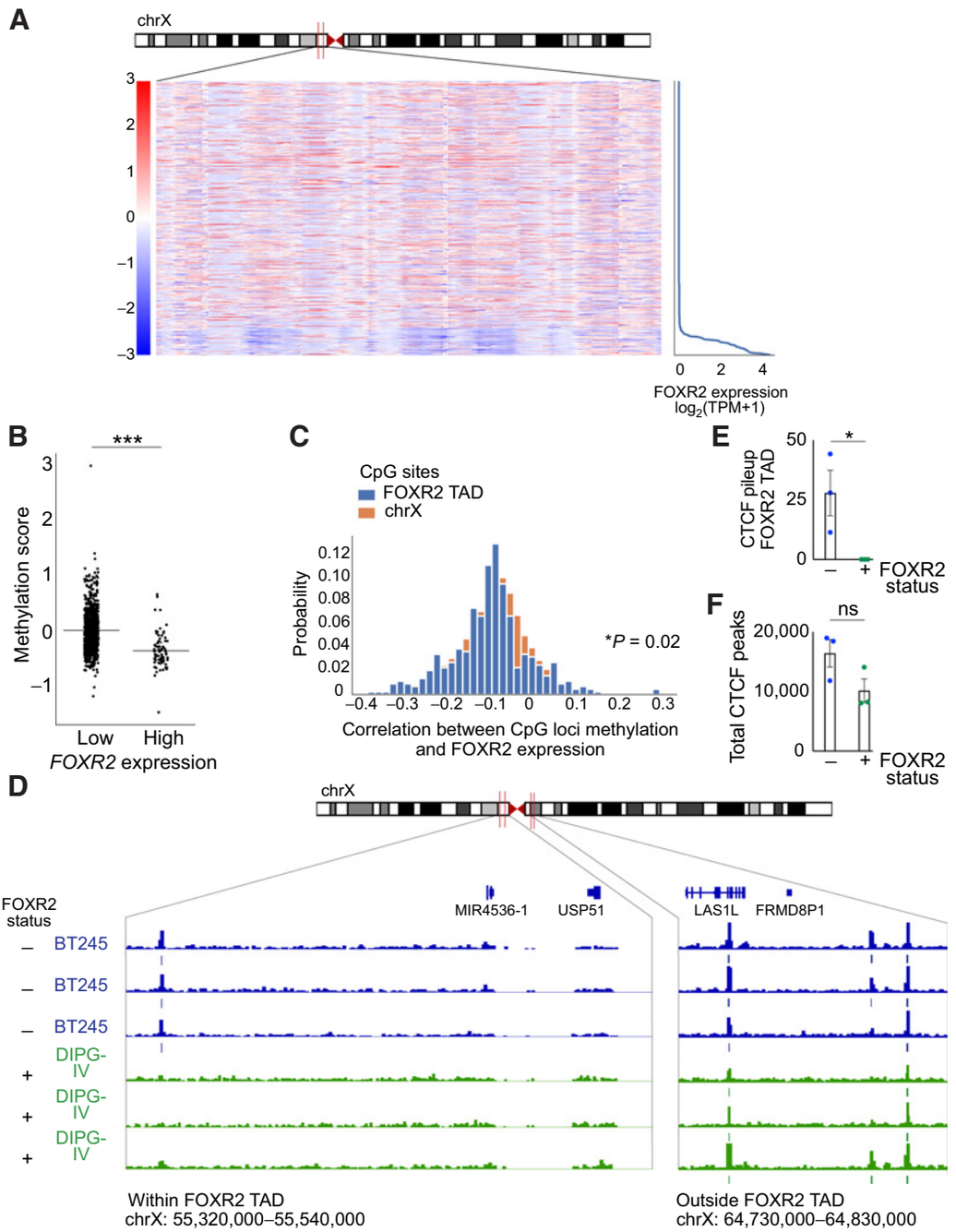

Figure 3.

FOXR2 is aberrantly expressed through epigenetic mechanisms. **A,** Heatmap of CCLE cell lines depicting z-scores (relative to mean of methylation for each CpG site) for all CpG sites within the FOXR2 TAD on the X chromosome as a function of *FOXR2* expression. *FOXR2*-expressing cell lines contain a 2-Mb region that is significantly hypomethylated relative to other regions of the X chromosome. *FOXR2*-expressing cell lines are delineated by *FOXR2* expression (right). **B,** Quantification of FOXR2 TAD methylation score for each CCLE cancer cell line ($P = 1.965e{-}15$, as determined by Welch *t* test). Each cell line is represented by an individual dot, and *FOXR2* expression (low vs. high) is indicated on the *x*-axis. **C,** Correlation between methylation at CpG loci and *FOXR2* expression (*x*-axis) and the probability of these correlations (*y*-axis). Blue, CpG sites within the *FOXR2* TAD; orange, the entire X chromosome. **D,** CTCF binding of the hypomethylated region shown in **A** that encompasses *FOXR2* in *FOXR2*-expressing DIPG-IV diffuse midline glioma (DMG; bottom) and non–*FOXR2*-expressing BT245 cells (top). Three independent replicates are shown for each cell line. Two regions are highlighted: within the FOXR2 TAD (chrX: 55,320,00–55,540,000; left) and outside of the FOXR2 TAD (chrX: 64,730,000–64,830,000; right). **E,** Quantification of the CTCF pileup specifically in the indicated region encompassing the FOXR2 TAD in three replicates of non–*FOXR2*-expressing cell lines (BT245) and three replicates of *FOXR2*-expressing DMG cells (DIPG-IV; $P = 0.0424$, unpaired *t* test). **F,** Quantification of total CTCF peaks across the genome in three replicates of non–*FOXR2*-expressing BT245 DMG cells and three replicates of *FOXR2*-expressing DIPG-IV DMG cells ($P = 0.1078$, unpaired *t* test). ns, not significant.

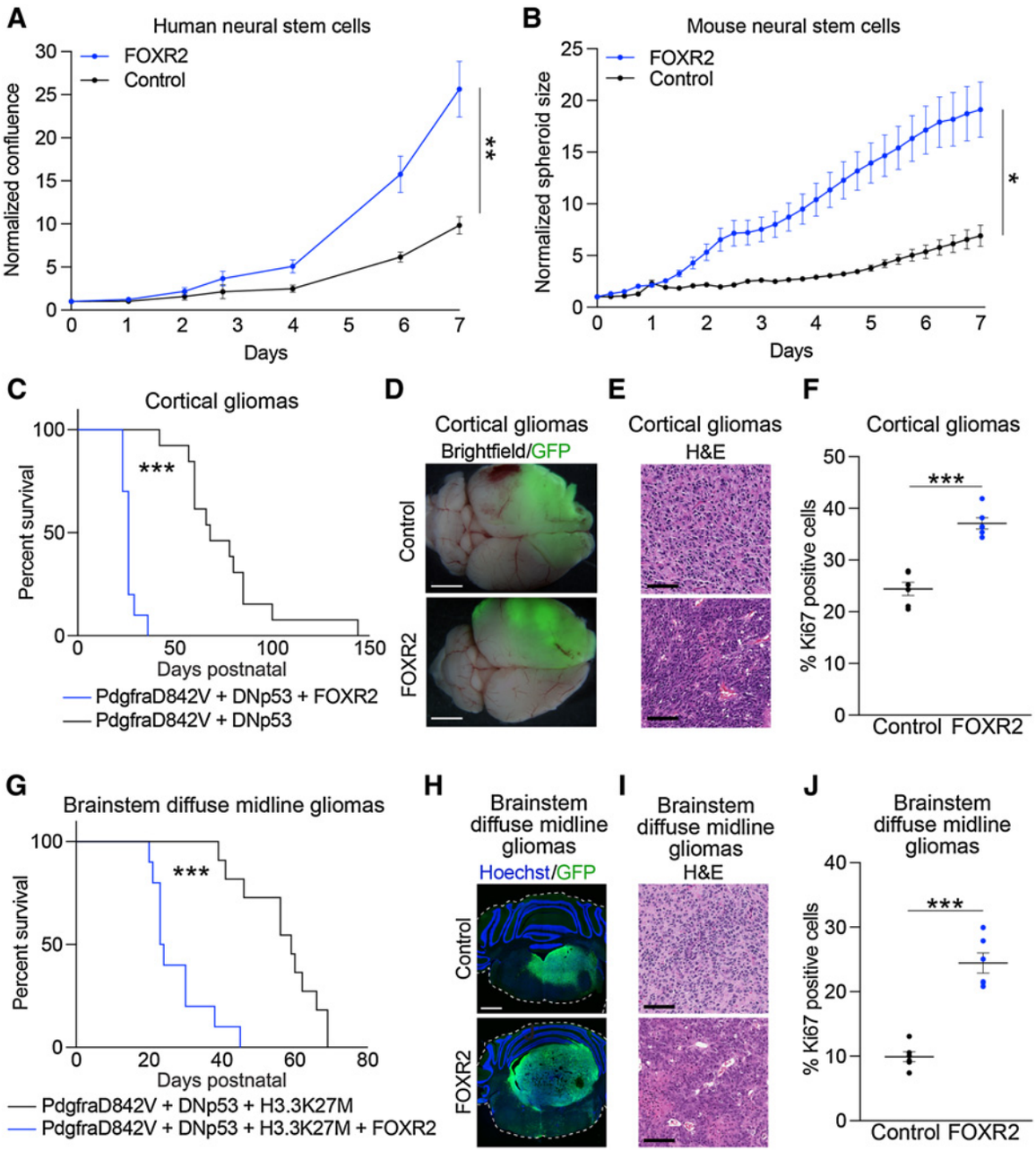

Figure 4.

FOXR2 is sufficient *in vitro* and *in vivo* to promote proliferation and tumor formation. **A,** Normalized confluence of H9 hNSCs expressing *FOXR2* relative to control. Values indicate mean ± SEM across three replicate experiments. **, $P < 0.01$, as determined by a two-tailed unpaired *t* test on day 7. **B,** Normalized spheroid size (relative to day 0) of mNSCs transduced with lentiviral vectors to induce expression of *FOXR2* or vector control. Values indicate mean ± SEM across three replicate experiments. *, $P < 0.05$, as determined by a two-tailed unpaired *t* test on day 7. **C,** Survival curves of control ($n = 13$) and *FOXR2*-expressing ($n = 10$) IUE pediatric high-grade glioma (PdgfraD842V + DNp53) mouse models. ***, $P < 0.0001$, as determined by the log-rank Mantel–Cox test. **D,** Representative whole-brain images of control and *FOXR2*-expressing IUE pediatric high-grade glioma (PdgfraD842V + DNp53) mouse models. GFP expression indicates the cortical location of IUE-targeted pediatric high-grade glioma models. Scale bar, 1 mm. **E,** Representative hematoxylin and eosin (H&E) staining of control and *FOXR2*-expressing IUE cortical gliomas. Scale bar, 100 μm. **F,** Percentage of Ki67-positive cells in tumors collected from control or *FOXR2*-expressing IUE cortical gliomas. Values indicate mean ± SEM from tumors obtained from six mice per condition. ***, $P < 0.0001$, as determined by a two-tailed unpaired *t* test. **G,** Survival curves of control ($n = 11$) and *FOXR2*-expressing ($n = 10$) IUE brainstem DMG (PdgfraD842V + DNp53 + H3.3K27M) mouse models. ***, $P < 0.0001$ as determined by log-rank Mantel–Cox test. **H,** Representative images of control and *FOXR2*-expressing IUE brainstem DMG models labeled with GFP (green) and counterstained with Hoechst (blue). GFP expression indicates the brainstem location of IUE-targeted DMG models. Hoechst stains nuclei as a marker of all cells. **I,** Representative hematoxylin and eosin staining of control and *FOXR2*-expressing IUE brainstem DMG models. Scale bar, 100 μm. **J,** Percentage of Ki67-positive cells in tumors collected from control or *FOXR2*-expressing IUE brainstem DMG models. Values indicate mean ± SEM from tumors obtained from six mice per condition. ***, $P < 0.0001$, as determined by a two-tailed unpaired *t* test.

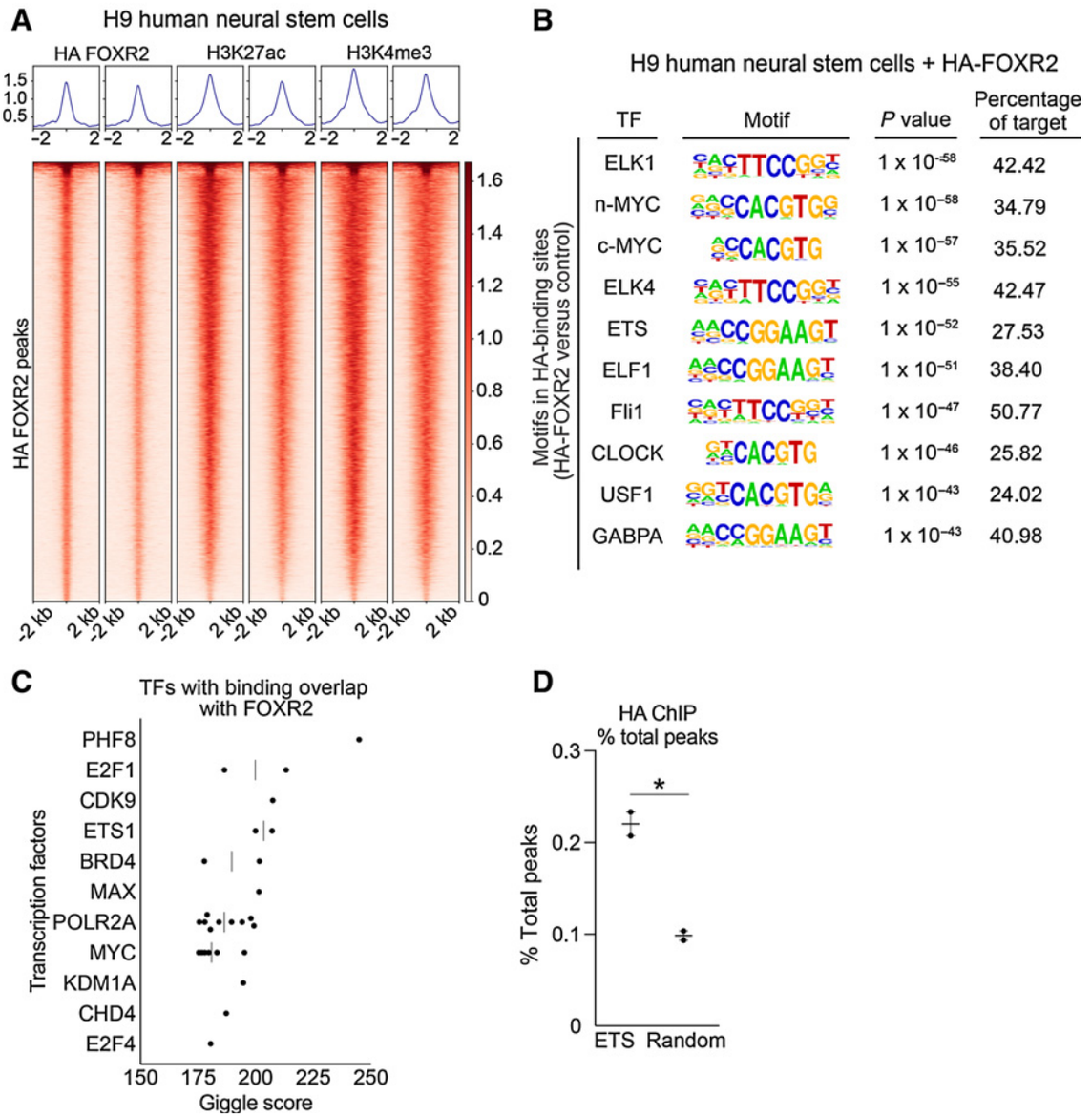

Figure 5.

FOXR2 is enriched for ETS motifs. **A,** Heatmaps of HA ChIP-seq peaks overlapping with H3K27ac and H3K4me3 peaks in H9 hNSCs expressing HA-FOXR2. Each row is centered on a HA-FOXR2 peak. The regions are rank ordered by the HA-FOXR2 signal. Intensity indicates average binding intensity at that site. **B,** Top 10 most significantly enriched known motifs from HA ChIP-seq in hNSCs expressing HA-FOXR2. Transcription factor, motif sequence, *P* value, and percentage of target sequences are shown. **C,** Top 11 TFs with significant binding overlap to HA-FOXR2 from Cistrome GIGGLE analysis. **D,** Percent of total peaks found in the 28 ETS family TFs compared with 28 randomly selected TFs across two replicate experiments. *, $P < 0.05$, as determined by a two-tailed unpaired *t* test.

anticorrelated compared with all other sites across the X chromosome ($P = 0.02$, Welch *t* test; **Fig. 3C**).

These findings suggest that the *FOXR2* locus is hypomethylated in *FOXR2*-expressing cancers and that this hypomethylation involves a broader region that includes *FOXR2*. We hypothesized that this region of hypomethylation may indicate the boundaries of the *FOXR2*-associated TAD. We, therefore, leveraged ChIP-seq, enriching for CTCF to compare CTCF insulator structure in *FOXR2*-expressing (SV negative) and non-FOXR2 DMG cancer cell lines (**Fig. 3D**). Indeed, *FOXR2*-expressing lines exhibited an altered CTCF binding profile within the hypomethylated region, exhibiting a paucity of additional CTCF binding between these peaks compared with non-*FOXR2*-expressing cells (**Fig. 3E**, $P < 0.05$, *t* test, Supplementary Table S3). Across the entire genome, the total number of CTCF peaks called in *FOXR2*-expressing tumors was not significantly different from the total number of CTCF peaks in non–*FOXR2*-expressing cells ($P > 0.05$, *t* test, **Fig. 3F**; Supplementary Table S3), revealing similar CTCF enrichment across experiments.

Taken together, these data nominate aberrant promoter activation by hypomethylation of the *FOXR2* TAD, and SVs to a lesser extent, as mechanisms through which cancers induce *FOXR2* expression.

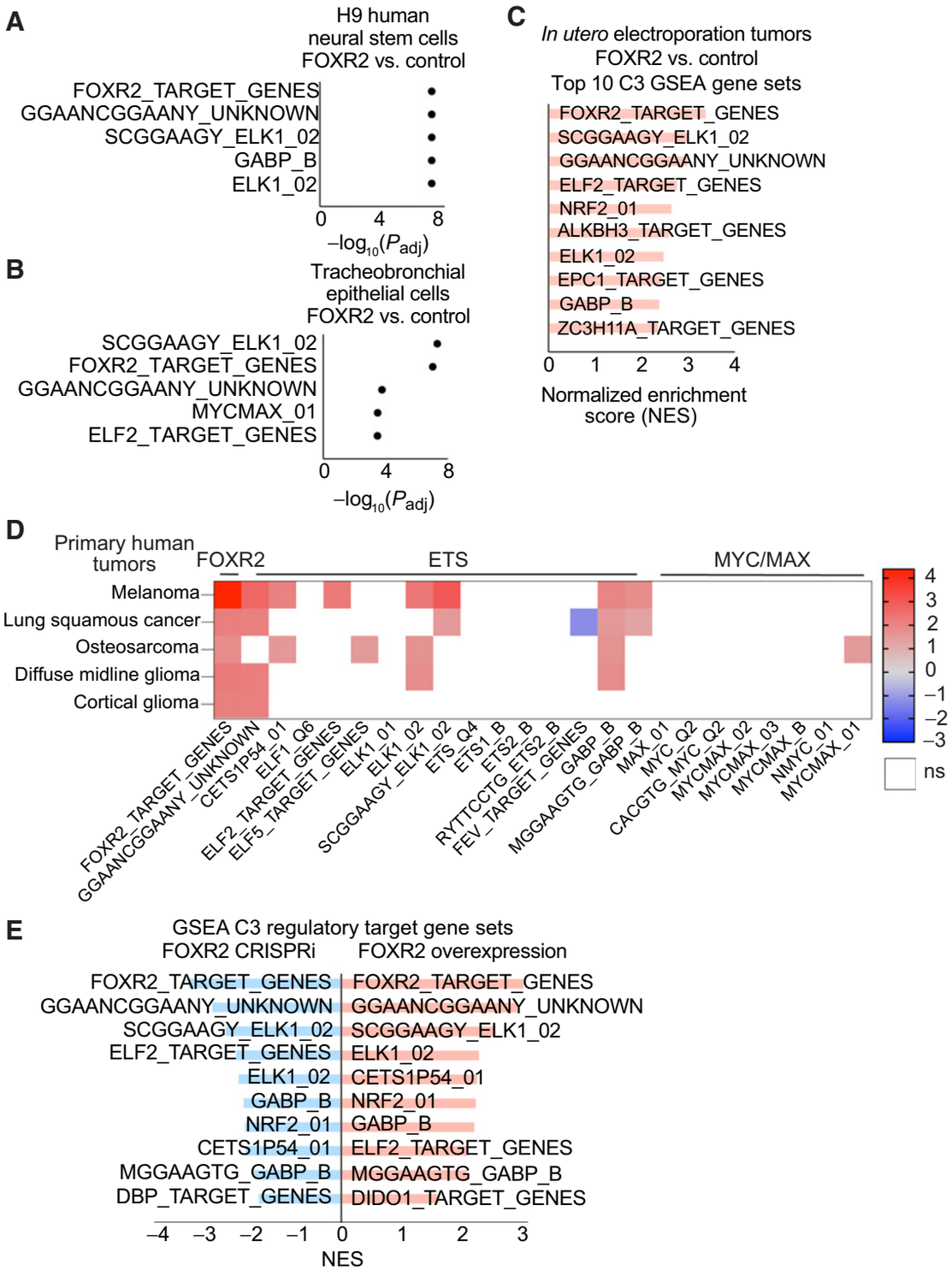

Figure 6.

FOXR2 specifically regulates ETS transcriptional circuits. **A,** GSEA of C3-regulatory target gene sets in *FOXR2*-expressing H9 hNSCs. The top five most significant (q value < 0.05) FOX, ETS, and MYC/MAX gene sets are plotted by $-\log_{10}(q$ value). **B,** GSEA of C3-regulatory target gene sets in *FOXR2*-expressing tracheobronchial epithelial cells (AALE). The top five most significant (q value < 0.05) FOX, ETS, and MYC/MAX gene sets are plotted by $-\log_{10}(q$ value). **C,** GSEA of C3-regulatory target gene sets in tumor models generated by IUE, comparing *FOXR2*-expressing glioma tumors to non–*FOXR2*-expressing controls. The top 10 most significant (q value < 0.05) gene sets are plotted by normalized enrichment score (NES). (*Continued on the following page.*)

FOXR2 expression is sufficient to enhance tumor formation

We next sought to evaluate whether *FOXR2* expression was sufficient to enhance cellular proliferation across multiple lineages. H9 NSCs (**Fig. 4A**), primary mNSCs (**Fig. 4B**), and immortalized tracheobronchial epithelial cells (AALE; Supplementary Fig. S4A; ref. 11) were transduced to ectopically express HA-tagged *FOXR2* (Supplementary Fig. S4A–S4D). Within each model, expression of *FOXR2* was associated with accelerated proliferation relative to vehicle controls ($P < 0.05$ for all comparisons, *t* test, **Fig. 4A** and **B**; Supplementary Fig. S4A; Supplementary Table S3).

FOXR2 expression is also sufficient to enhance gliomagenesis *in vivo*. As our genomic analyses revealed *FOXR2* expression in both cortical HGG and midline/brainstem DMG tumors, we evaluated whether FOXR2 was sufficient to enhance glioma formation in each of these locations. We first determined the effect of *FOXR2* expression using IUE-based models of hemispheric HGG created by expression of a constitutively active Pdgfra-mutant (Pdgfra-D842V) and dominant-negative TP53 (DNp53; refs. 38, 50). These models mirror alterations found in human gliomas (15, 51, 52) and we have previously shown that they recapitulate the human disease (38, 50). In this context, expression of *FOXR2* significantly enhanced glioma formation compared with the control conditions and was associated with reduced overall survival (**Fig. 4C**; $P < 0.0001$, log-rank Mantel–Cox test; Supplementary Table S3). *FOXR2*-expressing gliomas were anaplastic, with a marked increase in tumor cellularity and proliferation rate (**Fig. 4D–F**; $P < 0.0001$, unpaired *t* test; Supplementary Table S3).

Similarly, *FOXR2* expression enhanced tumor growth in the brainstem. We induced *FOXR2* expression in IUE DMG models expressing Pdgfra-D842V or wild-type Pdgfra (Pdgfra-WT) with DNp53 and H3.3K27M (38). Pdgfra-D842V IUE DMGs expressing *FOXR2* displayed reduced overall survival compared with Pdgfra-D842V IUE DMG control tumors ($P < 0.0001$, log-rank Mantel–Cox test; **Fig. 4G**; Supplementary Table S3), with large tumors developing in the brainstem that overtook most of the hindbrain area (**Fig. 4H**; Supplementary Fig. S4E). *FOXR2*-expressing gliomas exhibited multiple high-grade features, including necrosis, vascular changes, and increased growth and proliferation, as evidenced by increased Ki67 staining ($P < 0.0001$, unpaired *t* test; **Fig. 4I** and **J**; Supplementary Fig. S4F; Supplementary Table S3).

Expression of *FOXR2* in a second IUE DMG model with Pdgfra-WT mirrored these findings, displaying increased tumor growth and proliferation within transfected brainstem tumor cells ($P < 0.0001$, unpaired *t* test; Supplementary Fig. S4G–S4I; Supplementary Table S3). Moreover, all IUE DMG model tumor conditions retained lineage-defining markers of HGG/DMG including diffuse Olig2 (Supplementary Fig. S4J) and Gfap (Supplementary Fig. S4K) labeling, and immunofluorescent staining for *FOXR2* confirmed expression in *FOXR2* IUE-transfected conditions (Supplementary Fig. S4L).

Combined, these results support *FOXR2* to represent an oncogenic driver that is both necessary for proliferation and sufficient to enhance tumor formation.

FOXR2 co-opts ETS transcription factor motifs

Our findings show aberrant *FOXR2* expression is sufficient to exert oncogenic activity across multiple lineages. We thus sought to further elucidate the mechanisms through which FOXR2 enhances tumor formation, including mapping its downstream transcriptional targets, which have not been systematically characterized. To address this, we generated ChIP-seq roadmaps of FOXR2, H3K4me3 promoter, and H3K27ac binding sites across the genome in hNSCs transduced to express FOXR2. We identified an average of 1,553 FOXR2 (FDR < 0.1), 22,819 H3K4me3, and 23,376 H3K27ac binding peaks (FDR < 0.01; Supplementary Table S6). FOXR2 binding sites overlapped with transcriptionally active sites across the genome, including H3K4me3 promoter and H3K27ac enhancer peaks (**Fig. 5A**), with an enrichment of FOXR2 binding at promoter regions (Supplementary Fig. S5A).

The most enriched FOXR2 binding motifs were associated with the ETS family of TFs, comprising 6 of the top 10 most significantly enriched motifs (**Fig. 5B**; Supplementary Table S7). These included ELK1, ELK4, ETS, ELF1, Fli1, and GABPA ($P < 0.0001$ in each case). Moreover, motifs for the additional ETS TFs ETV1, ETS1, ETV2, ERG, SPDEF, EHF, and ELF5 were also significantly enriched ($P < 0.0001$ in each case). This unexpected finding raised the possibility that FOXR2 activates ETS family transcription programs. We further validated this by interrogating 13,006 previously analyzed ChIP-seq data sets using the Cistrome DB Toolkit to identify factors with significant binding overlap with FOXR2 binding sites (**Fig. 5C**; refs. 34–36, 42). This analysis compares peak enrichment across all ChIP-seq samples to identify those with the most similarity to user-defined peaks and found FOXR2 binding sites to significantly overlap with the ETS family transcription factor ETS1 (Supplementary Table S8).

The apparent association of FOXR2 with ETS transcriptional programs led us to reason that FOXR2 binding may be enriched at ETS family transcription factor genes themselves. Indeed, we observed ETS TFs to be associated with a higher proportion of total HA-FOXR2 binding peaks (±50 Kb of each gene) compared with 28 randomly selected non-ETS transcription factor controls ($P = 0.01$, *t* test; **Fig. 5D**; Supplementary Table S3).

FOXR2 activates ETS transcriptional programs

We performed transcriptome-wide RNA-seq to define transcriptional signatures associated with *FOXR2* expression and identified 7,023 genes and 1975 gene sets to be differentially expressed in *FOXR2*-expressing hNSCs (Supplementary Table S9, q threshold < 0.05; ref. 53). GSEA of the C3 regulatory target gene sets (54–56) confirmed FOXR2 to be the most differentially enriched gene set (q < 0.0001, **Fig. 6A**; Supplementary Fig. S5B–S5C; Supplementary Table S9).

(*Continued.*) **D,** Heatmap depicting relative expression of the FOXR2 target gene set, 15 ETS transcription factor gene sets, and 8 MYC/MAX gene sets within the C3 database in *FOXR2*-expressing versus non–*FOXR2*-expressing samples across different human cancers. Gradient depicts NES for each lineage, with red showing high enrichment, blue indicating negative enrichment, and white indicating no significant enrichment of each gene set. Human tumors include TCGA melanoma (SKCM) human tumors (total, $n = 472$; FOXR2, $n = 48$), TCGA-LUSC human tumors (total, $n = 551$; FOXR2, $n = 15$), osteosarcomas human tumors (total, $n = 150$; FOXR2, $n = 5$), human diffuse midline gliomas (DMGs; total, $n = 67$; FOXR2, $n = 5$), and human cortical gliomas (total, $n = 32$; FOXR2 = 6). All colored squares are significantly enriched or depleted with a *q* value < 0.05, with the exception of osteosarcoma, for which a *q*-value threshold of < 0.25 was applied. White squares are not significant based on this FDR threshold. **E,** GSEA of C3 regulatory target gene sets in *FOXR2*-expressing models (red, right), combining both H9 hNSCs and tracheobronchial epithelial cells (AALE). GSEA was generated by comparing hNSCs and AALE cells transduced with *FOXR2* relative to hNSCs and AALE cells transduced with a vector control ($n = 3$ replicates per condition). The top 10 most significant gene sets are plotted by NES with *q* value = 4.66E−8. GSEA of C3-regulatory target gene sets in *FOXR2* CRISPRi suppression models (blue, left), combining both DMG DIPG-IV and melanoma (SKCM) A375. Primary *FOXR2*-expressing cancer cell lines with *FOXR2* suppression transduced with CRISPRi targeting the Exon -3 promoter were compared with primary *FOXR2*-expressing cancer cell lines transduced with a CRISPRi control vector ($n = 3$ replicates per condition). The top 10 most significant gene sets are plotted by their NES with *q* value = 9.56E−9.

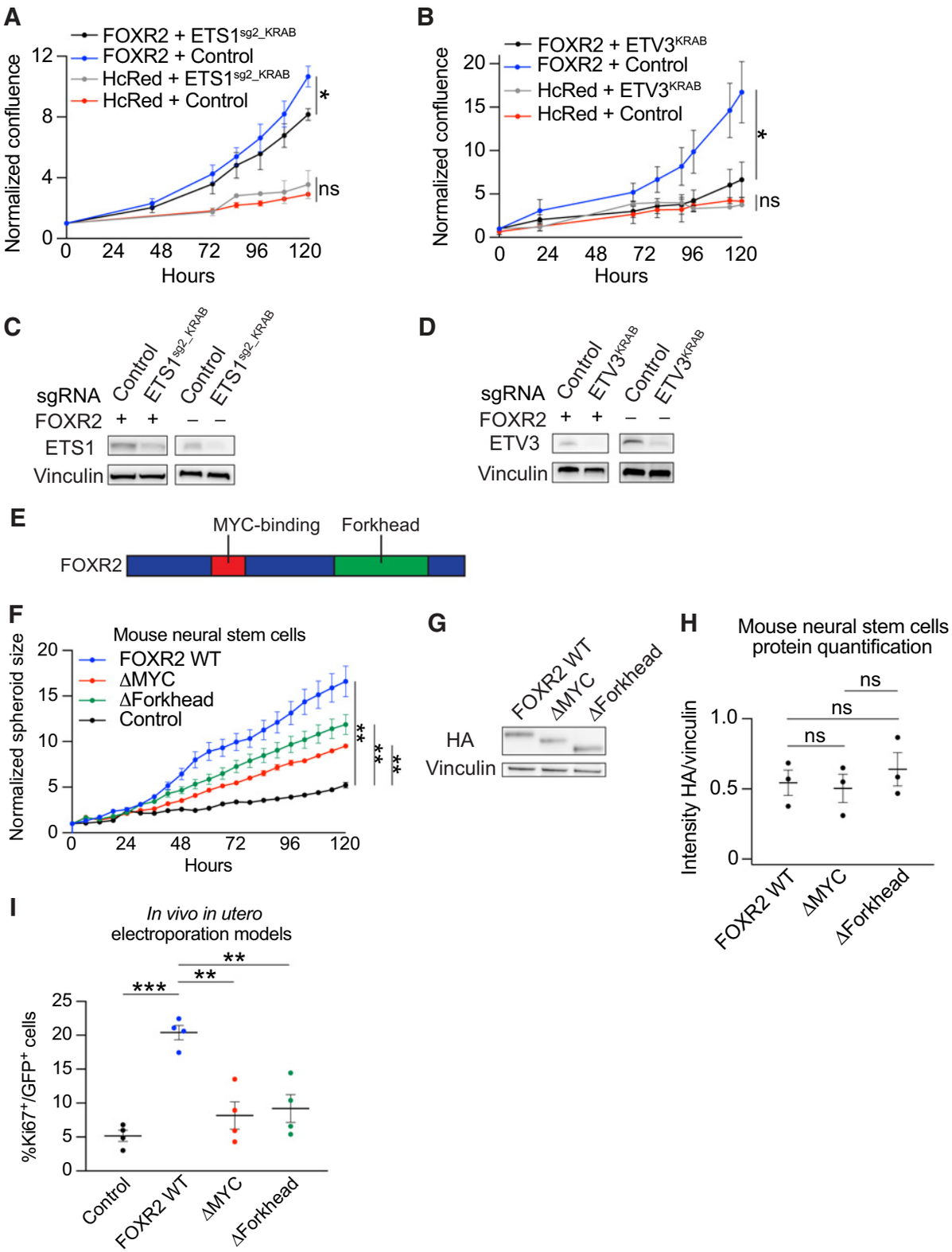

The next most significant pathway was GGAANCGGAANY_UNKNOWN ($q < 0.0001$), an ETS motif (57, 58). In total, 12 of the 15 ETS TF gene sets in the C3 database were significantly enriched in *FOXR2*-expressing hNSCs ($q < 0.05$). Of the 24 forkhead TF gene sets in the C3 database, only FOXR2 gene targets were significantly positively enriched in FOXR2-expressing hNSCs (Supplementary Fig. S5D), demonstrating the specificity of observed transcriptional programs to FOXR2.

These findings extended to lung tracheobronchial epithelial (AALE) cells (11). Within this lineage, we identified 8,096 genes and 1,989 gene sets to be differentially expressed in *FOXR2*-expressing AALE cells (Supplementary Table S10, q threshold <0.05). GSEA of the C3 regulatory target gene sets revealed the most enriched gene set to be associated with the ELK1 motif (q value <0.0001), an ETS transcription factor (**Fig. 6B**; Supplementary Fig. S5C). Of the 24 forkhead TF gene sets in C3, only FOXR2 gene targets were significantly enriched in AALE cells expressing *FOXR2*, consistent with our findings in hNSCs (Supplementary Fig. S5D). Six of the 15 ETS family C3 TF gene sets were significantly enriched in *FOXR2*-expressing AALE cells (Supplementary Table S10).

Indeed, when combined with transcriptional changes associated with *FOXR2* expression in hNSCs, 8 of the top 10 most differentially altered C3 gene sets are associated with ETS TFs (Supplementary Fig. S5C; Supplementary Table S11). However, within each of these lineages, individual ETS TFs are not highly represented within the top 100 most differentially expressed genes, suggesting that FOXR2 co-opts the activity of ETS regulatory circuits to a greater extent than regulating expressing of ETS TFs themselves. These results were further validated in our IUE tumor models, with FOXR2 and ETS TF family gene sets among the top enriched C3 regulatory target gene sets in *FOXR2*-expressing tumors (**Fig. 6C**).

ETS regulatory circuits are activated in primary *FOXR2*-expressing human tumors

Within cohorts of primary human tumors, including DMG, hemispheric gliomas, osteosarcomas, SKCM, and NSCLC, we found FOXR2 and ETS gene sets to be the most differentially regulated transcriptional programs in *FOXR2*-expressing compared with non–*FOXR2*-expressing tumors (**Fig. 6D**; Supplementary Fig. S3F). Within *FOXR2*-expressing DMGs (total DMGs $n = 67$, *FOXR2*-expressing $n = 5$), FOXR2 target genes were the most significantly enriched in the C3 database ($q < 0.05$). Only five C3 gene sets were significant with a q value < 0.05, including three ETS gene sets (**Fig. 6D**; Supplementary Fig. S5D; Supplementary Table S12). Similarly, within *FOXR2*-expressing non-midline, hemispheric gliomas (total $n = 32$, *FOXR2*-expressing $n = 6$), FOXR2 target genes and an ETS-associated gene set (**Fig. 6D**; Supplementary Fig. S5D; Supplementary Table S12) were the only two gene sets within the C3 database with q value < 0.05. Across SKCM (total $n = 472$, *FOXR2*-expressing $n = 48$), LUSC (total $n = 551$, *FOXR2*-expressing $n = 15$), and osteosarcoma (total $n = 150$, *FOXR2*-expressing $n = 5$) lineages, FOXR2 targets followed by ETS transcription programs also represented the most significantly enriched gene sets ($q < 0.0001$ for SKCM, LUSC; $q < 0.25$ for osteosarcoma, **Fig. 6D**; Supplementary Table S12). These findings were specific to comparisons between *FOXR2*-expressing and nonexpressing tumors. We did not observe similar enrichment of FOXR2 or ETS gene sets with random permutations of tumor labels keeping relative class sizes the same.

These data, generated across multiple contexts and lineages, demonstrate that ETS circuits represent the dominant transcriptional network activated by FOXR2.

Expression of *FOXR2* is necessary to maintain the transcription of ETS regulatory circuits

We characterized the transcriptomic changes following the suppression of *FOXR2* by CRISPRi of the Exon −3 promoter in DMG cells and found 1,120 genes and 4,267 gene sets to be differentially expressed (q threshold < 0.05; Supplementary Table S13). GSEA of the C3 regulatory target gene sets confirmed the FOXR2-associated pathway to be the most differentially depleted following *FOXR2* suppression (Supplementary Fig. S5E; Supplementary Table S13, $q < 0.0001$), followed by five ETS motifs or pathways gene sets. Indeed, nine of the 15 ETS gene sets were significantly depleted upon *FOXR2* knockdown. These findings extended to *FOXR2*-expressing melanoma (SKCM) cells in which suppression of *FOXR2* most significantly depleted FOXR2 targets and four ETS gene sets ($q < 0.0001$ in each case; Supplementary Fig. S5F; Supplementary Table S14).

When *FOXR2* knockdown data sets from both DMG and SKCM cells were combined, 440 genes and 4,963 gene sets were differentially expressed (Supplementary Table S15, $q < 0.05$). Within C3 gene sets, FOXR2 targets were most depleted and eight of the top 10 most significantly depleted gene sets were ETS gene sets ($q < 0.0001$ in each case; **Fig. 6E**; Supplementary Table S15).

Together, these data demonstrate that FOXR2 TF activity is sufficient and necessary to regulate ETS circuits within FOXR2-expressing lineages.

The ETS1 and ETV3 TFs are necessary for FOXR2-mediated proliferation in human NSCs

We next reasoned that activation of ETS transcription circuits is necessary for the oncogenic function of FOXR2. Leveraging hNSCs, we assessed the necessity of candidate ETS transcription factors in *FOXR2*-mediated proliferation, focusing on two specific ETS TFs,

Figure 7.

ETS TFs are necessary for *FOXR2*-mediated proliferation. **A,** Normalized confluence of H9 hNSCs expressing FOXR2 + vector control, FOXR2 + ETS1^{sg2_KRAB}, HcRed + vector control, and HcRed + ETS1^{sg2_KRAB}. Values indicate mean ± SEM across three replicate experiments. *, $P < 0.05$, as determined by a two-tailed unpaired t test on day 5. **B,** Normalized confluence of H9 hNSCs expressing FOXR2 + vector control, FOXR2 + ETV3^{KRAB}, HcRed + vector control, and HcRed + ETV3^{KRAB}. Values indicate mean ± SEM across three replicate experiments. *, $P < 0.05$, as determined by a two-tailed unpaired t test on day 5. **C,** Representative Western immunoblot depicting ETS1 protein levels in H9 hNSCs expressing FOXR2 + vector control, FOXR2 + ETS1^{sg2_KRAB}, HcRed + vector control, and HcRed + ETS1^{sg2_KRAB}. **D,** Representative Western immunoblot depicting ETV3 protein levels in H9 hNSCs expressing FOXR2 + vector control, FOXR2 + ETV3^{KRAB}, HcRed + vector control, and HcRed + ETV3^{KRAB}. **E,** Schematic depicting FOXR2 protein domains. The MYC-binding domain is indicated in red and forkhead DNA-binding domain is indicated in green. **F,** Growth of neurospheres (measured as spheroid size) of mNSCs expressing *FOXR2* WT relative to mNSCs expressing ΔMYC, ΔForkhead, and control, and normalized to day 0 values. Values indicate mean ± SEM across three replicate experiments. **, $P < 0.01$, as determined by two-tailed unpaired t tests. **G,** Representative Western immunoblot depicting HA-tagged FOXR2 protein levels in mNSCs expressing *FOXR2* WT, ΔMYC, and ΔForkhead. **H,** Quantification of HA protein expression in Western immunoblots performed using lysates derived from mNSC-transduced *FOXR2* WT, ΔMYC, and ΔForkhead. Values from three independent experiments and their mean ± SEM are shown. ns, not significant as determined by a two-tailed unpaired t test with $P > 0.05$. **I,** Percentage of GFP-positive cells that are Ki67-positive cells in control, *FOXR2* WT, ΔMYC, and ΔForkhead expressing IUE tumors. Values represent Ki67% positivity in four independent tumors per condition. Black horizontal line indicates the mean across all four tumors, with error bars representing SEM. **, $P < 0.01$; ***, $P < 0.001$ as determined by two-tailed unpaired t tests.

ETV3 and *ETS1*, that are upregulated in both *FOXR2*-expressing hNSCs and in FOXR2-expressing DMGs. In this model, knockdown of ETS1 and ETV3 resulted in attenuation of FOXR2-mediated proliferation compared with those transduced with nontargeting guides (**Fig. 7A–D**; Supplementary Fig. S6A–S6D; Supplementary Table S3). We conclude that expression of both ETS1 and ETV3 is required for FOXR2 to enhance cellular proliferation.

The FOXR2 forkhead domain is required for FOXR2-mediated transformation

FOXR2 has previously been described to exert oncogenesis through its ability to bind and stabilize MYC proteins (5, 7). Indeed, we found *FOXR2*-expressing glioma cells and mNSCs transduced to express FOXR2 to exhibit increased stability of MYC protein relative to non–FOXR2-expressing controls ($P < 0.05$, *t* test; Supplementary Fig. S6E–S6H; Supplementary Table S3). However, our findings suggest that FOXR2 also acts to transcriptionally activate ETS transcription circuits, which have also been implicated in oncogenesis. We, therefore, hypothesized that the FOXR2 forkhead domain is also required for its oncogenic effects.

To assess the relative contribution of the Forkhead and MYC domains in *FOXR2*-mediated proliferation mNSCs were transduced to express *FOXR2* transcripts in which we had deleted either the Forkhead (ΔForkhead) or MYC-binding (ΔMYC) domains, in addition to WT and vector controls (**Fig. 7E**). Consistent with our prior experiments, *FOXR2* WT rapidly accelerated the proliferation of cells relative to control ($P = 0.004$, *t* test, **Fig. 7F–H**; Supplementary Table S3). However, although mNSCs transduced with ΔForkhead exhibited increased growth compared with vector controls ($P < 0.05$, *t* test), the growth rate was attenuated compared with FOXR2 WT ($P = 0.003$, *t* test; Supplementary Table S3). Similarly, ΔMYC was associated with increased growth relative to vector controls, and attenuation of proliferation compared with *FOXR2* WT ($P < 0.05$ for each comparison, *t* test; **Fig. 7F**; Supplementary Table S3). The growth rate of mNSCs transduced with ΔForkhead did not differ from those transduced with ΔMYC ($P > 0.05$, *t* test). These findings suggest that both the forkhead and MYC domains are partially necessary for FOXR2-mediated transformation.

We validated these findings in our IUE glioma mouse models created by the concurrent expression of wild-type Pdgfra (Pdgfra-WT), dominant-negative p53 (DNp53), H3.3K27M, and *FOXR2* WT, ΔForkhead, ΔMYC, or vector control. When electroporated brains were collected two months post birth and analyzed to determine the effects of each condition on tumor cell proliferation, expression of ΔForkhead or ΔMYC domain mutants exhibited attenuated proliferation compared with *FOXR2* WT samples (**Fig. 7I**; $P < 0.05$ for both comparisons, *t* test; Supplementary Table S3), supporting our *in vitro* findings that both the Forkhead and MYC domains participate in the oncogenic function of *FOXR2*.

Discussion

We comprehensively mapped the spectrum of *FOXR2* expression across cancers and found aberrant activation across at least 70% of all cancer lineages, including both adult and pediatric cancers. We have systematically delineated the routes through which *FOXR2* is aberrantly expressed, uncovering a novel epigenetic mechanism in the majority of tumors. Moreover, we show that FOXR2 hijacks ETS transcription circuits to mediate its oncogenic effects, revealing a previously unknown cooperation between two major classes of TFs in driving cancer formation.

We have identified and functionally validated a promoter region that likely represents the canonical transcription start site of *FOXR2*. The novel FOXR2 promoters identified in this study reside in the noncoding region upstream of the annotated FOXR2 gene. This region has also been previously implicated in FOXR2-activating SVs in CNS and peripheral NBs, and in our study, in numerous lineages including gliomas, melanoma, and NSCLC. However, we show that epigenetic activation represents the most frequent path to *FOXR2* expression across all cancers. Moreover, we also observe this aberrant promoter to reside within a hypomethylated region on the X chromosome that encompasses *FOXR2*. This finding of specific hypomethylation in the region of the FOXR2 TAD is reminiscent of other genes on the X chromosome, such as cancer–testis antigens, whose aberrant expression has also been implicated in cancers (46, 47).

This analysis demonstrates that tumor types across lineages leverage multiple pathways, both epigenetic and genetic, to activate *FOXR2* expression. The fact that numerous cancer types, both adult and pediatric, have been selected for processes to activate *FOXR2* expression underscores its potency as an oncogenic driver. To this end, our work has functionally validated the sufficiency and necessity of the aberrant Exon −3 promoter region to drive *FOXR2* expression, and the necessity of *FOXR2* itself to mediate proliferation. Further, we show the sufficiency of FOXR2 to enhance cell growth and tumor formation in numerous models, both *in vitro* and *in vivo* and across lineages.

FOXR2 has previously been shown to regulate MYC/MYCN stability (4, 5, 7) and to promote activation of numerous pathways in various contexts, including FAK/SRC signaling (4), p27 pathway, WNT signaling, SHH activation (3), and epithelial-to-mesenchymal transition. However, there remains to be a consistent mechanism defined across cancer lineages. From our integrated analysis, we were particularly intrigued by the unifying theme that FOXR2 co-opts ETS motifs. Across experiments, model systems, and primary tumor types, FOXR2 expression was consistently linked to the regulation of ETS transcriptional circuits. Moreover, we found that ETS TFs are necessary for FOXR2-mediated transformation. These findings suggest that FOXR2 cooperates with at least two other families of TFs that themselves represent major oncogenes. MYC isoforms have been well documented to represent oncogenic drivers across many cancers (59), and activation of ETS TFs is a key event in Ewing's sarcoma (60), leukemia (61), prostate (62, 63), and other cancers (64, 65). However, our finding of associations between FOXR2 and ETS transcriptional activation broadens the mechanisms known to activate the latter in both adult and pediatric cancer types, and further studies are needed to delineate precisely how ETS TFs contribute to *FOXR2*-mediated oncogenesis (66, 67).

Several questions remain regarding the mechanisms through which FOXR2 and ETS TFs cooperate. Prior work in vascular development shows that normal endothelial cells can utilize a unique FOX:ETS motif where FOX and ETS TFs cooperate to bind at this enhancer element (68). Additionally, at the protein–protein level, many FOX proteins are known to cooperate with other TFs (69, 70) and even may cooperate with other FOX family members (9, 10). Further work should explore how FOXR2 physically interacts with ETS family members.

The lack of *FOXR2* expression across most normal tissues nominates it as an attractive tumor-specific therapeutic target. However, therapeutic disruption of FOXR2 and its association with MYC and ETS TFs remains a challenge. Our HA-FOXR2 ChIP-seq data demonstrate that FOXR2 colocalizes with enhancers and promoters. It is possible, therefore, that one therapeutic approach would be to

disrupt transcriptional complex formation (BETi, CDK7). Other novel strategies emerging include degradation by hijacking E3 machinery, although the mechanisms by which FOXR2 stability is regulated are presently unknown. ETS TFs could also be considered as a potential therapeutic target, particularly in light of work in sarcomas validating ETS inhibition. Ultimately, successful targeting of FOXR2 or its downstream effectors would have applicability in almost 10% of all human cancers, across a wide range of cancer subtypes.

Authors' Disclosures

J.W. Tsai reports grants from Alex's Lemonade Stand, St. Baldrick's Foundation (with support from Griffin's Guardians), Pedals for Pediatrics, Helen Gurley Brown Presidential Initiative, and NIH T32 training grant CA 136432-11 during the conduct of the study. F.P. Dubois reports grants and personal fees from Deutsche Forschungsgemeinschaft during the conduct of the study. D.S. Ziegler reports personal fees from Bayer, Amgen, Day One, Novartis, Alexion, FivepHusion, Accendatech, and AstraZeneca outside the submitted work. C.M. Kramm reports grants from Deutsche Kinderkrebsstiftung during the conduct of the study. S.S. Bielack reports personal fees from MAP Biopharma, Ipsen, Hoffmann La Roche, Bayer Healthcare, Boehringer Ingelheim, EISAI, and Eli Lilly outside the submitted work. J.M. McFarland reports other support from the Dependency Map Consortium during the conduct of the study. G. Getz reports personal fees from Scorpion Therapeutics and grants from IBM and Pharmacyclics outside the submitted work; in addition, G. Getz has a patent for SignatureAnalyzer-GPU pending. F. Aguet reports he is an employee of Illumina, Inc., since November 8, 2021. O. Witt reports grants from BVD, Day One, personal fees from BMS, Janssen, and Novartis outside the submitted work. D.T. Jones reports grants from German Consortium for Translational Cancer Research, German Cancer Aid (DKH), German Childhood Cancer Foundation (DKKS), BILD e.V. Ein Herz für Kinder, and German Federal Ministry of Education and Research (BMBF) during the conduct of the study. P. Bandopadhayay reports grants from Novartis Institute of Biomedical Research, Deerfield Therapeutics, and personal fees from QED therapeutics outside the submitted work. T. Phoenix reports grants from Michael Mosier Defeat DIPG Foundation, The ChadTough Foundation, Prayers from Maria Children's Cancer Foundation, Pediatric Brain Tumor Foundation, Department of Defense, and The Matthew Larson Foundation during the conduct of the study. No disclosures were reported by the other authors.

Authors' Contributions

J.W. Tsai: Conceptualization, data curation, formal analysis, validation, investigation, visualization, writing–original draft, writing–review and editing. **P. Cejas:** Formal analysis, investigation, visualization, writing–review and editing. **D.K. Wang:** Investigation. **S. Patel:** Investigation, writing–review and editing. **D.W. Wu:** Data curation, formal analysis, investigation, visualization, writing–review and editing. **P. Arounleut:** Investigation, writing–review and editing. **X. Wei:** Investigation, writing–review and editing. **N. Zhou:** Software, formal analysis, investigation, visualization, writing–review and editing. **S. Syamala:** Investigation, writing–review and editing. **F.P. Dubois:** Investigation, writing–review and editing. **A. Crane:** Resources, writing–review and editing. **K. Pelton:** Investigation, writing–review and editing. **J. Vogelzang:** Investigation, writing–review and editing. **C. Sousa:** Investigation. **A. Baguette:** Software, formal analysis, investigation, writing–review and editing. **X. Chen:** Software, investigation, visualization, writing–review and editing. **A.L. Condurat:** Resources, writing–review and editing. **S.E. Dixon-Clarke:** Investigation, writing–review and editing. **K.N. Zhou:** Investigation. **S.D. Lu:** Investigation. **E.M. Gonzalez:** Investigation, writing–review and editing. **M.S. Chacon:** Investigation. **J.J. Digiacomo:** Investigation. **R. Kumbhani:** Investigation. **D. Novikov:** Investigation. **J. Hunter:** Investigation. **M. Tsoli:** Resources, investigation, writing–review and editing. **D.S. Ziegler:** Resources, investigation, writing–review and editing. **U. Dirksen:** Resources, writing–review and editing. **N. Jager:** Resources, writing–review and editing. **G. Balasubramanian:** Resources, writing–review and editing. **C.M. Kramm:** Resources. **M. Nathrath:** Resources, writing–review and editing. **S. Bielack:** Resources, writing–review and editing. **S.J. Baker:** Resources, investigation, writing–review and editing. **J. Zhang:** Resources, data curation, investigation, writing–review and editing. **J.M. McFarland:** Resources, software, formal analysis, investigation, writing–review and editing. **G. Getz:** Resources, data curation. **F. Aguet:** Resources, data curation. **N. Jabado:** Resources, investigation, writing–review and editing. **O. Witt:** Resources, data curation, writing–review and editing. **S.M. Pfister:** Resources, data curation, writing–review and editing. **K.L. Ligon:** Resources, supervision, investigation, writing–review and editing. **V. Hovestadt:** Formal analysis, writing–review and editing. **C.L. Kleinman:** Data curation, software, supervision, writing–review and editing. **H. Long:** Formal analysis, supervision, investigation, writing–review and editing. **D.T. Jones:** Conceptualization, resources, data curation, supervision, investigation, writing–original draft, project administration, writing–review and editing. **P. Bandopadhayay:** Conceptualization, resources, supervision, investigation, writing–original draft, project administration, writing–review and editing. **T.N. Phoenix:** Conceptualization, resources, formal analysis, supervision, funding acquisition, validation, investigation, writing–original draft, writing–review and editing.

Acknowledgments

The authors thank and acknowledge Eric Smith for designing and illustrating **Fig. 1F**. They thank the members of the Bandopadhayay, Jones, and Phoenix Laboratories for thoughtful discussions regarding this work. The authors thank Drs. Scott Armstrong, Rameen Beroukhim, Bradley Bernstein, Myles Brown, John G. Doench, David Largaespada, Bo Kyung A. Seong, and Kimberly Stegmaier for their data brainstorming sessions. They thank Dr. Matthew Meyerson for AALE cells. The authors thank James W. Schwoebel for random number generation. They thank the following core facilities: Molecular Biology Core Facilities (MBCF) at DFCI, Center for Functional Cancer Epigenetics (CFCE) at DFCI, Flow Cytometry Core at DFCI, Genetic Perturbation Platform (GPP) at the Broad Institute, and Genomic Services at the Broad Institute. The Genotype-Tissue Expression (GTEx) Project was supported by the Common Fund of the Office of the Director of the NIH and by NCI, NHGRI, NHLBI, NIDA, NIMH, and NINDS. They thank the ENCODE Consortium and the Stamatoyannopoulos and Bernstein Laboratories for generating the ENCODE data sets utilized in this work. The results shown here are in part based upon data generated by the TCGA Research Network: https://www.cancer.gov/tcga. The authors would like to thank and acknowledge the following funding sources: The Giving for Gabi Fund (P. Bandopadhayay), The V Foundation for Cancer Research (P. Bandopadhayay), Michael Mosier Defeat DIPG Foundation (T.N. Phoenix and P. Bandopadhayay), The ChadTough Foundation (T.N. Phoenix and P. Bandopadhayay), The St. Baldrick's Foundation (J.W. Tsai), Prayers from Maria Children's Cancer Foundation (P. Bandopadhayay and T.N. Phoenix), Pediatric Brain Tumor Foundation (S. Dixon-Clarke, K.L. Ligon, P. Bandopadhayay, and T.N. Phoenix), Department of Defense Grant #CA171185 (T.N. Phoenix), Jared Branfman Sunflowers for Life Fund (P. Bandopadhayay), NIH R37 5R37CA255245-02 (P. Bandopadhayay), The Isabel V. Marxuach Fund for Medulloblastoma Research (P. Bandopadhayay), The Matthew Larson Foundation (T.N. Phoenix), Broad Institute Escape Velocity Award (P. Bandopadhayay), Alex's Lemonade Stand Foundation (J.W. Tsai and P. Bandopadhayay), We Love You Connie Foundation (P. Bandopadhayay, N. Jabado, and K.L. Ligon), Helen Gurley Brown Presidential Initiative (J.W. Tsai and P. Bandopadhayay), Friends of DFCI (P. Bandopadhayay), Griffin's Guardians (J.W. Tsai), Pedals for Pediatrics (J.W. Tsai), NIH T32 training grant CA 136432-11 (J.W. Tsai), Cure Brain Cancer Foundation (M. Tsoli and D.S. Ziegler), Robert Connor Dawes Foundation (P, Bandopadhayay, M. Tsoli, and D.S. Ziegler), Cancer Institute NSW Program Grant TPG2037 (M. Tsoli and D.S. Ziegler), UCGNI Pilot Award (T.N. Phoenix), German Cancer Aid DKH 70113419, 70112018 (U. Dirksen), Trettner Foundation T0355/31554/2018 (U. Dirksen), and Deutsche Kinderkrebsstiftung (C.M. Kramm). The INFORM project is financially supported by the German Consortium for Translational Cancer Research (DKTK), German Cancer Aid (DKH), the German Childhood Cancer Foundation (DKKS), the German Cancer Research Center (DKFZ), BILD e.V. Ein Herz für Kinder, the German Federal Ministry of Education and Research (BMBF), and a generous donation from the Scheu family. The DepMap project is partially funded by CTD2, the Achilles consortium, and The Carlos Slim Foundation in Mexico through the Slim Initiative for Genomic Medicine.

The costs of publication of this article were defrayed in part by the payment of page charges. This article must therefore be hereby marked *advertisement* in accordance with 18 U.S.C. Section 1734 solely to indicate this fact.

Note

Supplementary data for this article are available at Cancer Research Online (http://cancerres.aacrjournals.org/).

Received February 24, 2022; revised May 11, 2022; accepted June 28, 2022; published first July 8, 2022.

References

1. Myatt SS, Lam EW. The emerging roles of forkhead box (Fox) proteins in cancer. Nat Rev Cancer 2007;7:847–59.
2. Rahrmann EP, Watson AL, Keng VW, Choi K, Moriarity BS, Beckmann DA, et al. Forward genetic screen for malignant peripheral nerve sheath tumor formation identifies new genes and pathways driving tumorigenesis. Nat Genet 2013;45:756–66.
3. Koso H, Tsuhako A, Lyons E, Ward JM, Rust AG, Adams DJ, et al. Identification of FoxR2 as an oncogene in medulloblastoma. Cancer Res 2014;74:2351–61.
4. Beckmann PJ, Larson JD, Larsson AT, Ostergaard JP, Wagner S, Rahrmann EP, et al. Sleeping beauty insertional mutagenesis reveals important genetic drivers of central nervous system embryonal tumors. Cancer Res 2019;79:905–17.
5. Schmitt-Hoffner F, van Rijn S, Toprak UH, Mauermann M, Rosemann F, Heit-Mondrzyk A, et al. FOXR2 stabilizes MYCN protein and identifies non-MYCN-amplified neuroblastoma patients with unfavorable outcome. J Clin Oncol 2021;39:3217–28.
6. Sturm D, Orr BA, Toprak UH, Hovestadt V, Jones DTW, Capper D, et al. New brain tumor entities emerge from molecular classification of CNS-PNETs. Cell 2016;164:1060–72.
7. Li X, Wang W, Xi Y, Gao M, Tran M, Aziz KE, et al. FOXR2 interacts with MYC to promote its transcriptional activities and tumorigenesis. Cell Rep 2016;16:487–97.
8. Cirillo LA, Lin FR, Cuesta I, Friedman D, Jarnik M, Zaret KS. Opening of compacted chromatin by early developmental transcription factors HNF3 (FoxA) and GATA-4. Mol Cell 2002;9:279–89.
9. Seo S, Kume T. Forkhead transcription factors, Foxc1 and Foxc2, are required for the morphogenesis of the cardiac outflow tract. Dev Biol 2006;296:421–36.
10. Shu W, Lu MM, Zhang Y, Tucker PW, Zhou D, Morrisey EE. Foxp2 and Foxp1 cooperatively regulate lung and esophagus development. Development 2007;134:1991–2000.
11. Bass AJ, Watanabe H, Mermel CH, Yu S, Perner S, Verhaak RG, et al. SOX2 is an amplified lineage-survival oncogene in lung and esophageal squamous cell carcinomas. Nat Genet 2009;41:1238–42.
12. Kume T. The cooperative roles of Foxc1 and Foxc2 in cardiovascular development. Adv Exp Med Biol 2009;665:63–77.
13. Cancer Genome Atlas Research N, Weinstein JN, Collisson EA, Mills GB, Shaw KR, Ozenberger BA, et al. The Cancer Genome Atlas Pan-Cancer analysis project. Nat Genet 2013;45:1113–20.
14. Barretina J, Caponigro G, Stransky N, Venkatesan K, Margolin AA, Kim S, et al. The cancer cell Line Encyclopedia enables predictive modelling of anticancer drug sensitivity. Nature 2012;483:603–7.
15. Dubois F, Shapira O, Greenwald N, Zack T, Wala J, Tsai J, et al. Structural variants shape driver combinations and outcomes in pediatric high-grade glioma. Nat Cancer 2022. doi 10.21203/rs.3.rs-389596/v1.
16. van Tilburg CM, Pfaff E, Pajtler KW, Langenberg KPS, Fiesel P, Jones BC, et al. The pediatric precision oncology INFORM registry: clinical outcome and benefit for patients with very high-evidence targets. Cancer Discov 2021;11:2764–79.
17. McLeod C, Gout AM, Zhou X, Thrasher A, Rahbarinia D, Brady SW, et al. St. Jude Cloud: a pediatric cancer genomic data-sharing ecosystem. Cancer Discov 2021;11:1082–99.
18. Worst BC, van Tilburg CM, Balasubramanian GP, Fiesel P, Witt R, Freitag A, et al. Next-generation personalised medicine for high-risk paediatric cancer patients: the INFORM pilot study. Eur J Cancer 2016;65:91–101.
19. Cerami E, Gao J, Dogrusoz U, Gross BE, Sumer SO, Aksoy BA, et al. The cBio cancer genomics portal: an open platform for exploring multidimensional cancer genomics data. Cancer Discov 2012;2:401–4.
20. Mounir M, Lucchetta M, Silva TC, Olsen C, Bontempi G, Chen X, et al. New functionalities in the TCGAbiolinks package for the study and integration of cancer data from GDC and GTEx. PLoS Comput Biol 2019;15:e1006701.
21. Silva TC, Colaprico A, Olsen C, D'Angelo F, Bontempi G, Ceccarelli M, et al. TCGA workflow: analyze cancer genomics and epigenomics data using Bioconductor packages. F1000Res 2016;5:1542.
22. Colaprico A, Silva TC, Olsen C, Garofano L, Cava C, Garolini D, et al. TCGAbiolinks: an R/Bioconductor package for integrative analysis of TCGA data. Nucleic Acids Res 2016;44:e71.
23. Grossman RL, Heath AP, Ferretti V, Varmus HE, Lowy DR, Kibbe WA, et al. Toward a shared vision for cancer genomic data. N Engl J Med 2016;375:1109–12.
24. Consortium GT. The Genotype-Tissue Expression (GTEx) project. Nat Genet 2013;45:580–5.
25. Sloan CA, Chan ET, Davidson JM, Malladi VS, Strattan JS, Hitz BC, et al. ENCODE data at the ENCODE portal. Nucleic Acids Res 2016;44:D726–32.
26. Tsherniak A, Vazquez F, Montgomery PG, Weir BA, Kryukov G, Cowley GS, et al. Defining a cancer dependency map. Cell 2017;170:564–76.
27. Broad Institute DM. DepMap 21Q3 Public. 2021.
28. Cornwell M, Vangala M, Taing L, Herbert Z, Koster J, Li B, et al. VIPER: visualization pipeline for RNA-seq, a Snakemake workflow for efficient and complete RNA-seq analysis. BMC Bioinf 2018;19:135.
29. Cancer Cell Line Encyclopedia C, Genomics of Drug Sensitivity in Cancer C. Pharmacogenomic agreement between two cancer cell line data sets. Nature 2015;528:84–7.
30. Li H, Handsaker B, Wysoker A, Fennell T, Ruan J, Homer N, et al. The sequence alignment/map format and SAMtools. Bioinformatics 2009;25:2078–9.
31. Krueger F, Andrews SR. Bismark: a flexible aligner and methylation caller for bisulfite-seq applications. Bioinformatics 2011;27:1571–2.
32. Akalin A, Kormaksson M, Li S, Garrett-Bakelman FE, Figueroa ME, Melnick A, et al. methylKit: a comprehensive R package for the analysis of genome-wide DNA methylation profiles. Genome Biol 2012;13:R87.
33. Qin Q, Mei S, Wu Q, Sun H, Li L, Taing L, et al. ChiLin: a comprehensive ChIP-seq and DNase-seq quality control and analysis pipeline. BMC Bioinf 2016;17:404.
34. Mei S, Qin Q, Wu Q, Sun H, Zheng R, Zang C, et al. Cistrome data browser: a data portal for ChIP-Seq and chromatin accessibility data in human and mouse. Nucleic Acids Res 2017;45:D658–D62.
35. Zheng R, Wan C, Mei S, Qin Q, Wu Q, Sun H, et al. Cistrome data browser: expanded datasets and new tools for gene regulatory analysis. Nucleic Acids Res 2019;47:D729–D35.
36. Li S, Wan C, Zheng R, Fan J, Dong X, Meyer CA, et al. Cistrome-GO: a web server for functional enrichment analysis of transcription factor ChIP-seq peaks. Nucleic Acids Res 2019;47:W206–W11.
37. Ramirez F, Dundar F, Diehl S, Gruning BA, Manke T. deepTools: a flexible platform for exploring deep-sequencing data. Nucleic Acids Res 2014;42:W187–91.
38. Patel SK, Hartley RM, Wei X, Furnish R, Escobar-Riquelme F, Bear H, et al. Generation of diffuse intrinsic pontine glioma mouse models by brainstem-targeted in utero electroporation. Neuro Oncol 2020;22:381–92.
39. Phoenix TN, Temple S. Spred1, a negative regulator of Ras-MAPK-ERK, is enriched in CNS germinal zones, dampens NSC proliferation, and maintains ventricular zone structure. Genes Dev 2010;24:45–56.
40. Consortium EP. An integrated encyclopedia of DNA elements in the human genome. Nature 2012;489:57–74.
41. Davis CA, Hitz BC, Sloan CA, Chan ET, Davidson JM, Gabdank I, et al. The encyclopedia of DNA elements (ENCODE): data portal update. Nucleic Acids Res 2018;46:D794–801.
42. Layer RM, Pedersen BS, DiSera T, Marth GT, Gertz J, Quinlan AR. GIGGLE: a search engine for large-scale integrated genome analysis. Nat Methods 2018;15:123–6.
43. Qi LS, Larson MH, Gilbert LA, Doudna JA, Weissman JS, Arkin AP, et al. Repurposing CRISPR as an RNA-guided platform for sequence-specific control of gene expression. Cell 2013;152:1173–83.
44. McFarland JM, Ho ZV, Kugener G, Dempster JM, Montgomery PG, Bryan JG, et al. Improved estimation of cancer dependencies from large-scale RNAi screens using model-based normalization and data integration. Nat Commun 2018;9:4610.
45. De Smet C, Lurquin C, Lethe B, Martelange V, Boon T. DNA methylation is the primary silencing mechanism for a set of germ line- and tumor-specific genes with a CpG-rich promoter. Mol Cell Biol 1999;19:7327–35.
46. Scanlan MJ, Simpson AJ, Old LJ. The cancer/testis genes: review, standardization, and commentary. Cancer Immun 2004;4:1.
47. Simpson AJ, Caballero OL, Jungbluth A, Chen YT, Old LJ. Cancer/testis antigens, gametogenesis and cancer. Nat Rev Cancer 2005;5:615–25.
48. Ehrlich M. DNA hypomethylation, cancer, the immunodeficiency, centromeric region instability, facial anomalies syndrome and chromosomal rearrangements. J Nutr 2002;132:2424S–9S.
49. Gu H, Smith ZD, Bock C, Boyle P, Gnirke A, Meissner A. Preparation of reduced representation bisulfite sequencing libraries for genome-scale DNA methylation profiling. Nat Protoc 2011;6:468–81.

50. Wei X, Meel MH, Breur M, Bugiani M, Hulleman E, Phoenix TN. Defining tumor-associated vascular heterogeneity in pediatric high-grade and diffuse midline gliomas. Acta Neuropathol Commun 2021;9:142.
51. Mackay A, Burford A, Carvalho D, Izquierdo E, Fazal-Salom J, Taylor KR, et al. Integrated molecular meta-analysis of 1,000 pediatric high-grade and diffuse intrinsic pontine glioma. Cancer Cell 2017;32:520–37.
52. Wu G, Diaz AK, Paugh BS, Rankin SL, Ju B, Li Y, et al. The genomic landscape of diffuse intrinsic pontine glioma and pediatric non-brainstem high-grade glioma. Nat Genet 2014;46:444–50.
53. Subramanian A, Tamayo P, Mootha VK, Mukherjee S, Ebert BL, Gillette MA, et al. Gene set enrichment analysis: a knowledge-based approach for interpreting genome-wide expression profiles. Proc Natl Acad Sci U S A 2005;102:15545–50.
54. Kolmykov S, Yevshin I, Kulyashov M, Sharipov R, Kondrakhin Y, Makeev VJ, et al. GTRD: an integrated view of transcription regulation. Nucleic Acids Res 2021;49:D104–D11.
55. Yevshin I, Sharipov R, Kolmykov S, Kondrakhin Y, Kolpakov F. GTRD: a database on gene transcription regulation-2019 update. Nucleic Acids Res 2019;47:D100–D5.
56. Yevshin I, Sharipov R, Valeev T, Kel A, Kolpakov F. GTRD: a database of transcription factor binding sites identified by ChIP-seq experiments. Nucleic Acids Res 2017;45:D61–D7.
57. Xie X, Lu J, Kulbokas EJ, Golub TR, Mootha V, Lindblad-Toh K, et al. Systematic discovery of regulatory motifs in human promoters and 3' UTRs by comparison of several mammals. Nature 2005;434:338–45.
58. Chatterjee R, Zhao J, He X, Shlyakhtenko A, Mann I, Waterfall JJ, et al. Overlapping ETS and CRE Motifs ((G/C)CGGAAGTGACGTCA) preferentially bound by GABPalpha and CREB proteins. G3 (Bethesda) 2012;2:1243–56.
59. Schaub FX, Dhankani V, Berger AC, Trivedi M, Richardson AB, Shaw R, et al. Pan-cancer alterations of the MYC oncogene and its proximal network across the Cancer Genome Atlas. Cell Syst 2018;6:282–300.
60. Crompton BD, Stewart C, Taylor-Weiner A, Alexe G, Kurek KC, Calicchio ML, et al. The genomic landscape of pediatric Ewing sarcoma. Cancer Discov 2014;4:1326–41.
61. Peeters P, Raynaud SD, Cools J, Wlodarska I, Grosgeorge J, Philip P, et al. Fusion of TEL, the ETS-variant gene 6 (ETV6), to the receptor-associated kinase JAK2 as a result of t(9;12) in a lymphoid and t(9;15;12) in a myeloid leukemia. Blood 1997;90:2535–40.
62. Tomlins SA, Laxman B, Dhanasekaran SM, Helgeson BE, Cao X, Morris DS, et al. Distinct classes of chromosomal rearrangements create oncogenic ETS gene fusions in prostate cancer. Nature 2007;448:595–9.
63. Clark JP, Cooper CS. ETS gene fusions in prostate cancer. Nat Rev Urol 2009;6:429–39.
64. Seth A, Watson DK. ETS transcription factors and their emerging roles in human cancer. Eur J Cancer 2005;41:2462–78.
65. Sizemore GM, Pitarresi JR, Balakrishnan S, Ostrowski MC. The ETS family of oncogenic transcription factors in solid tumours. Nat Rev Cancer 2017;17:337–51.
66. Hollenhorst PC, McIntosh LP, Graves BJ. Genomic and biochemical insights into the specificity of ETS transcription factors. Annu Rev Biochem 2011;80:437–71.
67. Findlay VJ, LaRue AC, Turner DP, Watson PM, Watson DK. Understanding the role of ETS-mediated gene regulation in complex biological processes. Adv Cancer Res 2013;119:1–61.
68. De Val S, Chi NC, Meadows SM, Minovitsky S, Anderson JP, Harris IS, et al. Combinatorial regulation of endothelial gene expression by ets and forkhead transcription factors. Cell 2008;135:1053–64.
69. Ono M, Yaguchi H, Ohkura N, Kitabayashi I, Nagamura Y, Nomura T, et al. Foxp3 controls regulatory T-cell function by interacting with AML1/Runx1. Nature 2007;446:685–9.
70. Schuur ER, Loktev AV, Sharma M, Sun Z, Roth RA, Weigel RJ. Ligand-dependent interaction of estrogen receptor-alpha with members of the forkhead transcription factor family. J Biol Chem 2001;276:33554–60.